



Aggregates and their distributions determined from LOPC observations made using an autonomous profiling float

Colleen M. Petrik^{a,*}, George A. Jackson^a, David M. Checkley Jr.^b

^a Department of Oceanography, Texas A&M University, College Station, TX 77843, USA

^b Scripps Institution of Oceanography, University of California, San Diego, La Jolla, CA 92093, USA

ARTICLE INFO

Article history:

Received 1 September 2012

Received in revised form

7 December 2012

Accepted 30 December 2012

Available online 9 January 2013

Keywords:

Particle distributions

Marine snow

Particle counter

Vertical flux

Zooplankton

ABSTRACT

The vertical flux of particles in the ocean drives the movement of organic carbon to the deep ocean. We have been studying the distribution and flux of these particles using the SOLOPC, a profiling Lagrangian (SOLO) float with a Laser Optical Particle Counter (LOPC). We have been able to distinguish between aggregate-like and zooplankton-like particles with diameters > 2 mm but needed a way to separate the smaller particles into aggregates and zooplankton. Observations included a lognormal-shaped fraction in the normalized volume distribution similar to that observed in results for simulations of particles in the euphotic zone. By fitting a lognormal distribution to the volume spectrum of particles with diameters ≤ 2 mm, we have been successful at making a separation of marine snow material from other, presumably living, particles. The particle volumes derived using the separations are positively correlated with fluorescence, particulate organic carbon, and the volume of larger particles classified as aggregate-like, which supports the conclusion that these particles are truly aggregates, in some cases derived from phytoplankton. The residual volumes (total less the above fit) are highly correlated with the volumes of large, zooplankton-like particles. Downward velocities of the aggregate fraction calculated from time series of particle profiles are consistent with previous estimates of particle settling rates ($20\text{--}70\text{ m d}^{-1}$). We now have a tool to estimate aggregate distributions, properties, and vertical fluxes in the euphotic zone, including when and where they change.

© 2013 Elsevier Ltd. All rights reserved.

1. Introduction

Particles and their motions relative to water (falling, rising, swimming) create distinctive biological and chemical zonation in the ocean. Such particles range from living organisms to aggregates containing mixtures of dead and living material. One such particle type observed by divers and cameras is known as marine snow; it can be composed of a mixture of plankton, detritus, and inorganic materials. Most aggregates originate from primary production in the euphotic zone and may form by coagulation or fecal pellet production, and can be fragmented by turbulence, remineralized by attached microbes, repackaged and redistributed by zooplankton feeding, or sink from the euphotic zone to the underlying mesopelagic. The resulting movement of particles out of the euphotic zone is a key part of the biological carbon pump that moves carbon out of the atmosphere and into the deep ocean.

* Corresponding author. Tel.: +1 508 274 8620.

E-mail addresses: cmpetrik@alaska.edu (C.M. Petrik), gjackson@tamu.edu (G.A. Jackson), dcheckley@ucsd.edu (D.M. Checkley Jr.).

¹ Present affiliation: School of Fisheries and Ocean Sciences, University of Alaska Fairbanks. Present address: Alaska Fisheries Science Center, NOAA NMFS, 7600 Sand Point Way NE, Seattle, WA 98115, USA.

The importance of particles in mediating oceanic biological and chemical processes has stimulated the development of techniques to detect and characterize particles automatically. Such techniques tend to have been developed separately by the aggregate and the plankton communities, although their instruments often detect both types of particles (e.g., Ashjian et al., 2001 (VPR); Checkley et al., 2008 (LOPC); Picheral et al., 2010 (UVP)). One such instrument, the Laser Optical Particle Counter (LOPC), was developed to measure zooplankton concentrations but also measures concentrations of aggregates (Herman et al., 2004; Jackson and Checkley, 2011). The LOPC has been attached to an autonomous Lagrangian profiling float to make the SOLOPC (Checkley et al., 2008). The SOLOPC allows sampling of particle distributions that are highly variable in time and space at scales relevant to them.

The LOPC measures the attenuation of particles passing through a light sheet sensed by multiple photodiode elements (Herman et al., 2004). When a *small* particle occludes all or part of 1 or 2 photodiode elements (single element particle; SEP) the LOPC estimates its equivalent spherical diameter (d_{esd} ; see Table 1 for all notation) and then adds a count to the appropriate size bin. In this case, d_{esd} is the diameter of an opaque sphere that attenuates the same amount of light. For *larger* particles that span at least 3 photodiode elements

Table 1Notation. All volumes based on d_{esd} . 1 ppm = 1 mm³ L⁻¹ = 1 cm³ m⁻³.

Symbol	Meaning	Typical units
a	Fractal constant	g cm ⁻¹
C	Cost function	–
d	Particle diameter	cm
d_{esd}	Particle equivalent spherical diameter	cm
d_{od}	Particle occluded diameter (width)	cm
d_{μ}	Aggregate particle median diameter	cm
\hat{d}_{esd}	Estimate of d_{esd} as function of d_{od} for fractal particles	cm
F_V	Particle volumetric vertical flux	m d ⁻¹
f	Fractal dimension	–
f_{1i}	Penalty parameter in C	–
f_2	Penalty parameter in C	–
f_3	Penalty parameter in C	–
m	Particle mass	g
$N(d)$	Number concentration of particles > d	cm ⁻³
N_{BV}^2	Seawater density gradient	s ⁻¹
$n(d)$	Differential number spectrum, in terms of d	cm ⁻⁴
n_{agg}	n resulting from the lognormal fitting	cm ⁻⁴
n_{res}	n for the non-fit particles, $n_{tot} - n_{agg}$	cm ⁻⁴
n_{tot}	n for all particles in a sample (SEPs and MEPs)	cm ⁻⁴
V	Volume of an individual particle	cm ³
V_T	Total particulate volume	ppm
V_{agg}	Total volume of fitted y_g fraction	ppm
V_{res}	Total volume of residual fraction	ppm
V_{sno}	Total volume of sno -particles	ppm
V_{tot}	Total volume of all particles (SEPs and MEPs)	ppm
V_{zoo}	Total volume of zoo -particles	ppm
ν	Settling rate	m d ⁻¹
ν_{xc}	Cross-correlation derived settling rate	m d ⁻¹
$\bar{\nu}$	Average settling rate	m d ⁻¹
y_g	Normal curve fit to nVd spectrum	–
μ	Parameter for y_g distribution	ln(cm)
σ	Parameter for y_g distribution	ln(cm)
σ_t	Seawater density	kg m ⁻³

(multiple element particles; MEPs), there is an additional measurement of diameter, the occluded diameter (d_{od}), the number of 1 mm light beams a particle occludes either partially or completely while passing through the light sheet. Thus, the LOPC provides a single measurement, based on opacity and size, for an SEP and data on both opacity and size for each MEP. Such data have been used to classify the larger particles into either marine snow or zooplankton (Jackson and Checkley, 2011). The information about the two particle groups can be combined to describe the particle distribution across the entire size range of d_{esd} .

The first SOLOPC deployments off Southern California tested the hypothesis that diel variation in primary production results in diel variation in abundance of aggregates, derived from phytoplankton (Checkley et al., 2008). The observations of particle size and distribution were consistent with a conceptual model of daytime phytoplankton production, followed by aggregation of phytoplankton and detritus, and then loss of aggregates by sinking and grazing. Estimates of particle flux in relation to the distribution of large copepods suggested possible grazing on the sinking particles.

The hypothesis that zooplankton control the flux of particulate matter to the mesopelagic was explored further by Jackson and Checkley (2011) with additional SOLOPC deployments, and by classifying the larger particles as aggregate-like and zooplankton-like based on their opacity and d_{esd} . The two different diameters of MEPs provide sufficient information to distinguish aggregates from zooplankton. For relatively opaque zooplankton, d_{esd} and d_{od} are similar. In contrast, marine snow particles are more amorphous and transparent and d_{esd} is substantially less than d_{od} . Jackson and Checkley (2011) separated MEPs into marine snow-like and zooplankton-like particles by using the values of

Table 2Details of SOLOPC deployments. lat_0 and $long_0$ are the latitude and longitude at deployment; t_d is the deployment duration.

Cruise	Deploy	ID	Launch d	lat_0	$long_0$	Dives	t_d (h)
Sproul05	1	SP05	28-Sep-05	33.0°N	–118.0°E	63	67
NewHorizon06	1	NH06	14-Sep-06	34.3°N	–121.1°E	86	100
Sproul07	1	SP07_1	23-Mar-07	34.8°N	–117.6°E	9	8
	2	SP07_2	23-Mar-07	32.8°N	–117.6°E	12	11
Thompson07	1	TH07_1	4-Apr-07	34.3°N	–120.9°E	70	93
	2	TH07_2	9-Apr-07	33.6°N	–123.1°E	72	83
	4	TH07_4	16-Apr-07	34.2°N	–121.2°E	76	99
Knorr08	1	BL08	2-May-08	61.2°N	–25.4°E	10	21
Gatekeeper	1	GK10_1	11-Jul-10	36.8°N	–122.1°E	41	44
	2	GK10_2	14-Jul-10	37.0°N	–123.3°E	192	210
	3	GK10_3	17-Jul-10	36.8°N	–122.1°E	31	33
	4	GK10_4	19-Jul-10	36.8°N	–122.0°E	8	9
	5+6	GK10_7	20-Jul-10	36.8°N	–122.1°E	61	72

d_{esd} and d_{od} in the manner described below. The method only worked for MEPs, particles with d_{od} of 3 mm and larger. How, then, do we classify particles with smaller values of d_{od} ?

We noticed a characteristic peak in the particle volume spectra for $d_{esd} < 1$ mm at most depths from the profiles of all SOLOPC deployments. Observations of aggregates produce similar Gaussian-shaped volume spectra. The volume size spectra of particles measured with a Coulter Counter during a chain-forming diatom bloom had such normal-shaped peaks (Kranck and Milligan, 1988). Also, a mesocosm experiment of aggregate formation from algae had a particle volume spectrum similar to a normal distribution, especially after 9 days into the experiment (Jackson, 1995). We hypothesized that the characteristic peak in our particle volume spectra was aggregates, and that small zooplankton caused the deviations from a smooth Gaussian. Consequently, we fit normal curves as a function of $\ln d_{esd}$ (lognormal as a function of d_{esd}) to this peak to isolate the aggregate particles.

We have developed a method for separating aggregates from zooplankton over the entire instrument size range. In this paper we describe the separation technique, compare the properties of these separated particles with those of aggregates, and apply it to describe temporal and spatial properties of these particles. To do so, we summarize results from multiple SOLOPC deployments, followed by a detailed analysis for one deployment, GK10_2, that was deployed offshore of Monterey Bay and approached the California Current. We then discuss the implications of this new method and the results of its application.

2. Methods

2.1. Data collection

Vertical profiles of particle size and abundance were collected with a SOLOPC (Checkley et al., 2008). The SOLOPC also measures temperature and salinity as a function of depth with a CTD, and backscatter and/or chlorophyll *a* fluorescence with WET Labs ECO Puck BBTOC and/or FLTOC sensors. We used the calibrations provided by WET Labs to convert FLTOC sensor readings to fluorescence-based chlorophyll concentration.

There are the equivalent of 70 beams, each 1 mm wide, sensed in the LOPC light sheet. The sensory area perpendicular to the flow is 49 cm² (Herman et al., 2004). SEPs were assigned a d_{esd} , which was used to add a count to the appropriate size bin. Every 3 s, the number of SEPs in each bin was recorded and then rezeroed. The minimum d_{esd} for an SEP was 0.09 mm. Each MEP

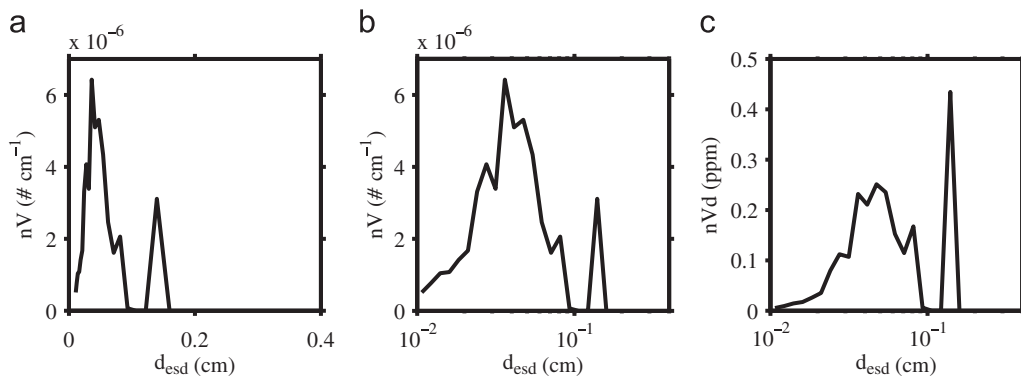


Fig. 1. Effect of displaying the same volumetric spectrum in different ways. (a) Volume spectrum $n_{tot}V$ as a function of d_{esd} . (b) Volume spectrum, $n_{tot}V$ as a function of $\ln d_{esd}$. (c) Normalized volume spectrum $n_{tot}Vd$ (ppm) as a function of $\ln d_{esd}$. The area under the curve between two values of d_{esd} is proportional to the total particle volume in that size range for a and c, but not b.

had multiple properties recorded, from which the d_{esd} and d_{od} were calculated when the data were processed using standard algorithms (Herman et al., 2004; Checkley et al., 2008). Unless otherwise indicated, d used here refers to d_{esd} .

The SOLOPC floats have been deployed off the coast of California on a number of cruises, in conditions that range from upwelling eutrophic to oligotrophic, as well as one brief deployment in the North Atlantic (Table 2). Water was sampled from the surface to 100 m depth. To avoid contamination of the LOPC with bubbles, we discarded particle data collected in the upper 5 m. The cycle time for each dive depended on conditions, but was typically about 1 h.

There were also water samples collected from 3 to 8 depths from CTD rosette casts made on the accompanying ship. These were analyzed for particulate organic carbon (POC) and/or particulate organic nitrogen (PON) concentrations following the CCE-CalCOFI methods (<http://cce.lternet.edu/data/methods/POCN/>). 1 L of seawater was filtered on precombusted Whatman GF/F 25 mm glass fiber filters under low vacuum pressure (40 mm Hg) and stored in liquid nitrogen at sea and in a -20°C freezer ashore until analyzed. Samples were acidified, dried and analyzed by high-temperature combustion (1000°C) on an ECS 4010 CHNSO Analyzer.

The Gatekeeper (GK) cruise off Monterey, California had the most intensive and extensive set of measurements. The GK10_2 deployment during the cruise was our longest deployment, lasting more than 10 d, and is the focus of the most intensive analysis in this paper. Further information about the deployment is in the results Section 3.3.1.

2.2. LOPC data analysis

2.2.1. Calculation of spectra

The number concentration of objects larger than d is denoted by $N(d)$. The number spectrum $n(d)$ is given by

$$n = -\frac{dN}{dd} \quad (1)$$

Within a small size interval Δd , the number of particles ΔN is given by

$$\Delta N \approx -n \cdot \Delta d \quad (2)$$

For spherical particles, the particle volume $V = (\pi/6)d^3$; the total volume of particles within a small size range Δd is given by $nV\Delta d$. nV is also the volume spectrum, the distribution of particle volume as a function of d . When the volume distribution

is plotted against a linear d -axis (Fig. 1a), the area under the nV curve between any two values of d is proportional to total particle volume within that size range (e.g., Jackson and Checkley, 2011). Plotting nV as a function of $\ln d$ distorts the curve by stretching out regions with smaller values of d and shrinking those with larger values, making it easier to distinguish the contribution of smaller particles but destroying the proportionality between area under the curve and total particle volume (Fig. 1b). Multiplying the volume distribution by d to plot nVd as a function of $\ln d$ compensates for this distortion so that the area under the curve is again proportional to the total volume (Fig. 1c). The quantity nVd is unitless; the total particulate volume is also unitless and represents the fraction of a volume occupied by particles. A typical total fractional volume is 1×10^{-6} , which is equivalent to $1 \text{ cm}^3 \text{ m}^{-3} = 1 \text{ part per million (ppm)}$.

We accumulated particle counts in 5 m depth intervals between 5 and 100 m. We calculated n_{tot} for each depth interval as a function of d using Eq. (2) and logarithmic diameter bins such that the upper value of d was 1.1447 times the lower value. This choice meant that values of particle volumes at the upper size of a bin were 1.5 times those at the lower. The subscript *tot* indicates that the spectrum was calculated using the combined SEP and MEP particle types and includes all particles. The $n_{tot}Vd$ values were calculated by multiplying the values of n_{tot} by $(\pi/6)d_i^4$, where d_i was the midpoint of the i th bin size range. For example, in deployment GK10_2 there were 43 diameter bins describing a spectrum, with values of d_i between 106 μm and 3.12 cm.

2.2.2. Fitting procedure

We fit normal curves as a function of $\ln d$ to the characteristic peak in the $n_{tot}Vd$ spectra in an attempt to isolate the particles that contributed to it from those that did not. We hypothesized that this curve would describe the aggregate distribution. If $x = \ln d$, then the fitting function has the form

$$y_g = V_{agg} \frac{1}{\sigma\sqrt{2\pi}} e^{-(x-\mu)^2/2\sigma^2} \quad (3)$$

where μ and σ describe the distribution peak and width, and V_{agg} is the total volume of particles covered by the distribution. The resulting number spectrum is then $n_{agg} = y_g V^{-1} d^{-1}$. Since y_g is a normal distribution with respect to $\ln d$, it is a lognormal distribution with respect to d , and e^μ is the median diameter of the particles in the lognormal distribution. We define $d_\mu = e^\mu$ since it carries the dimensional information of diameter (cm), and use this notation to discuss the median diameter of the particles in the lognormal y_g fraction.

For each $n_{tot}Vd$ spectrum, we estimated the values of μ , σ , and V_{agg} that provided the best fit to the spectrum by minimizing a cost function C by using the MATLAB *fminsearch* function. The primary method minimized

$$C = \sum_i \left(1 + 50f_{1i} \frac{(nVd(x_i) - y_g(x_i))^2}{i^2} \right) + 50f_2 + 50f_3 \quad (4)$$

where $x_i = \ln d_i$, $y_g(x_i)$ was the value of Eq. (3) at x_i , $f_{1i} = 1$ if $nVd(x_i) < y_g(x_i)$ and 0 otherwise, $f_2 = 1$ if $d_\mu > 0.09$ cm and 0 otherwise, and $f_3 = 1$ if $\sigma > 1.5$ and 0 otherwise. The variables f_{1i} , f_2 , and f_3 were used to penalize the cost function if y_g became greater than $n_{tot}Vd$ or if the values of d_μ and σ became too large. The i^2 term provided greater weight to the distribution of smaller particles.

A modified method (“fixed” method) was used when the first did not converge, when $d_\mu > 0.081$ cm, or $\sigma > 1.35$. In these cases the values of d_μ and σ were interpolated from the closest depths with acceptable parameter values. The value for V_{agg} was determined by minimizing C given these interpolated values of μ and σ .

2.2.3. Calculation of fractal dimension and separation of MEPs into sno-particles and zoo-particles

The diameter of any particle varies with the technique used to measure it. A measurement that uses particle mass to estimate diameter, such as d_{esd} , can yield a significantly smaller diameter than a technique that uses the particle outline. The difference between the two can be particularly large because particle porosity increases a particle's width without adding mass. Outline-based diameter measurements have often been related to particle mass, m , by using fractal scaling

$$m = ad^f \quad (5)$$

where f is the fractal dimension and a is a constant (e.g., Kilps et al., 1994; Jackson et al., 1995, 1997).

We used a modified version of the technique of Jackson and Checkley (2011) to calculate f for the large particles (MEPs) of each deployment and then to classify these particles as either marine snow-like *sno*-particles or zooplankton-like *zoo*-particles (their *s*- and *z*-particles) using the particle d_{esd} and d_{od} values (Fig. 2). The method involved the fitting of a curve to the maximum in the two-dimensional histogram describing the distributions of particles sorted by their d_{esd} and d_{od} values. We altered the technique by only using regions of the d_{esd} – d_{od} space where there were at least 5 particles in a size bin. The value of d_{esd} for any value of d_{od} calculated from this procedure, \hat{d}_{esd} , was used to define a boundary between *sno*-particles and *zoo*-particles, with any particle having a value of $d_{esd} < 1.5\hat{d}_{esd}$ considered a *sno*-particle, and any particle larger considered a *zoo*-particle. This was a more restrictive criterion than in Jackson and Checkley (2011), which used $d_{esd} < 2\hat{d}_{esd}$.

2.3. Estimation of settling velocities and fluxes

2.3.1. Using particle size distributions

The total particulate volume V_T (ppm) is

$$V_T = \int nV dd = \int nVd d(\ln d) \quad (6)$$

Similarly, if a particle's settling velocity, v ($m d^{-1}$), is a function of particle diameter, the total volumetric flux F_V ($m d^{-1}$) is

$$F_V = \int nVv dd = \int nVdv d(\ln d) \quad (7)$$

The average settling speed is then

$$\bar{v} = F_V/V_T \quad (8)$$

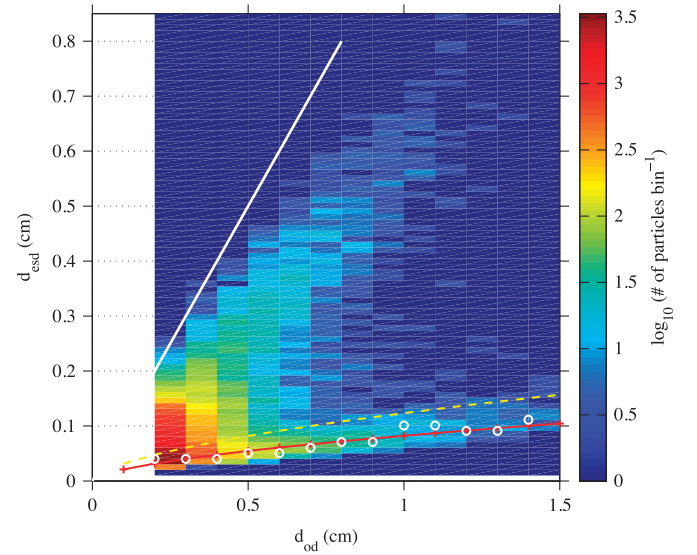


Fig. 2. Two-dimensional histogram of the number of particles in a size bin showing the relationship between occluded diameter (d_{od}) and estimated spherical diameter (d_{esd}) for GK10_2. The solid line (white line in web version) indicates where $d_{od} = d_{esd}$; the line with pluses (+) (red line) shows \hat{d}_{esd} as a function of d_{od} ; the dashed yellow line equals $1.5\hat{d}_{esd}$ and represents the boundary between particles classified as *zoo*-particles (above) and those classified as *sno*-particles (below). Small white circles indicate values used to determine the fractal dimension, here 1.77, as a step to calculate \hat{d}_{esd} . We interpret the two lobes, one above and one below the dashed yellow line, as representing zooplankton and marine snow, respectively.

We numerically integrated Eqs. (6) and (7) using y_g and the relationship for $v(d)$ in Jackson et al. (2005) to estimate \bar{v} for the normally distributed particle fraction.

2.3.2. Using changes in distribution of particle volume

We estimated the cross-correlation sequence of the time series of total particulate volume of the y_g fraction, V_{agg} , at one depth with those deeper for the 24 dives that followed it. For each dive pair, a particle velocity was estimated as the depth interval between the two depth bins divided by the time between dives. The mean settling rate v_{xc} was the average of those velocities having significant correlations ($p < 0.05$).

3. Results

3.1. Comparison of different fitting procedures

The results of the fitting procedures can be seen for a typical profile, here profile 191 from deployment GK10_2 (Gatekeeper cruise, deployment 2), with a detailed look at 7.5, 12.5 and 17.5 m (Fig. 3). The $n_{tot}Vd$ distributions at the three depths all have local maxima near $d = 500 \mu m$. The primary fitting procedure isolates the peaks at 7.5 and 17.5 m, but not at 12.5 m (Fig. 3a–c). At 12.5 m, the value of d_μ exceeds the maximum allowed, as the procedure is attracted to the maximum in $n_{tot}Vd$ distribution at $d \sim 1–2$ mm. The fixed procedure forces the parameters at 12.5 m to be within the allowable range and is centered on the small local maximum around $d = 500 \mu m$. In none of these cases does the normal shape match the $n_{tot}Vd$ distribution exactly. This could be because it is not the best shape or because there are zooplankton within the size range. In all cases, the difference in volume from fitting the peaks precisely is small.

In this profile, there was a general decrease in all the parameters from the surface to about 42.5 m (Fig. 3d–f). Below 42.5 m the

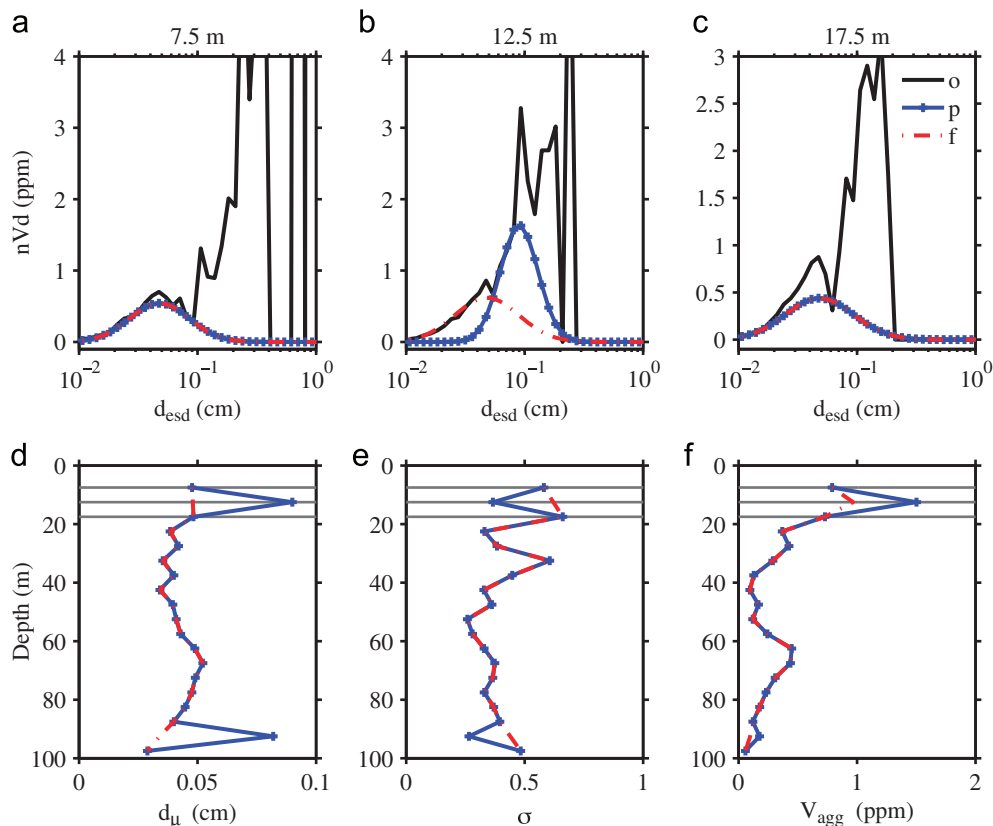


Fig. 3. Examples of nVd spectra and the y_g fits estimated by the two fitting methods at (a) 7.5, (b) 12.5, and (c) 17.5 m depth. Depth profiles of the parameter values (d) d_μ (cm), (e) σ , and (f) V_{agg} (ppm). The horizontal lines in panels (d–f) represent the depths shown in panels (a–c). Line key is in the legend in (c) where o: original ($n_{tot}Vd$), p: primary, f: fixed. Results for dive #191 of deployment GK10_2.

value of σ generally increased with depth while there were maxima at 62.5–72.5 m for V_{agg} and d_μ followed by another decrease (Fig. 3d–f). The changes in d_μ were relatively gradual, with the exception of spikes in d_μ at 12.5 and 97.5 m using the primary method that were smoothed by the fixed procedure (Fig. 3d). The fixed procedure smoothed the profiles of σ and V_{agg} (Fig. 3e, f), but not as much as for d_μ .

A comparison of the results with and without the fixed correction shows that there were relatively few differences. For GK10_2, the range of d_μ was 0.025 to 0.09 cm; for σ it was about 0.1–0.9. There were no values of σ large enough to trigger the fixed method. Values of $d_\mu > 0.081$ cm resulted in reduced values of 0.03–0.06 cm for the fixed method. There was little difference between values of total volume for the primary and fixed methods ($r=0.998$), although there were slight reductions in V_{agg} for the fixed method corresponding to the reduced d_μ values. The differences between the two fitting methods exemplified using deployment GK10_2 are representative of all the deployments. We present only the results from the fixed method, as it better fit the characteristic peaks $d < 1$ mm in the $n_{tot}Vd$ spectra in all deployments.

3.2. Properties of the Gaussian fraction

The particle fraction in the Gaussian fit and described by μ , σ , and V_{agg} we designate the y_g fraction; the rest, described by the distribution $n_{res}Vd = n_{tot}Vd - n_{agg}Vd$, we designate the residual fraction. Most, but not all, of the particle volume for $d_{esd} < 1$ mm was in the y_g fraction, while almost all of the particle volume for larger particles was in the residual fraction (e.g., Fig. 4). Note that while we were fitting the distributions calculated for all particles combined, SEPs, and MEPS, the Gaussian peak was

effectively constrained to cover particles less than 1 mm by the fitting procedure.

To determine if the y_g -residual separation had isolated distinctive particle types, we calculated the correlation between V_{agg} and volumes of different particle types, including all particles (V_{tot}), *sno*-particles (V_{sno}), *zoo*-particles (V_{zoo}), and the difference between (residual of) total and aggregate volumes (V_{res}). We also compared V_{agg} to fluorescence from the SOLOPC float and to nearby POC measurements. For most deployments, the total volume of the y_g fraction estimate was highly correlated with measures related to aggregates (Tables 3 and 4).

3.2.1. Comparison with the *sno*-particle and *zoo*-particle fractions

The small correlation ($r=0.43$; Table 3) between V_{agg} and the total particle volume, V_{tot} , for the combined data set of all deployments suggests that the fitting procedure produced a distinct fraction within the particle size spectrum. This low r value is replicated in correlations between V_{agg} and V_{tot} from individual deployments (Table 4). The correlation between the residual volume, V_{res} , and V_{tot} was larger, $r=0.99$ (Table 3), and is a reflection that V_{agg} was a small fraction of the total whose removal did not appreciably change the volume in most cases.

When the data for all deployments were combined, V_{agg} was most highly correlated with the *sno*-particle volume V_{sno} ($r=0.85$; Table 3) and was weakly correlated with the *zoo*-particle volume V_{zoo} ($r=0.34$). Within a deployment, the correlations between V_{agg} and V_{sno} ranged from a low of 0.29 for GK10_1 to a high of 0.96 for GK10_4, with a mean of r from all deployments of 0.71 (Table 4). Given the fact that V_{sno} includes only the larger MEPS, it is not surprising that GK10_1 had the smallest mean value of d_μ and GK10_4 the largest (Table 5). The correlations between V_{agg} and

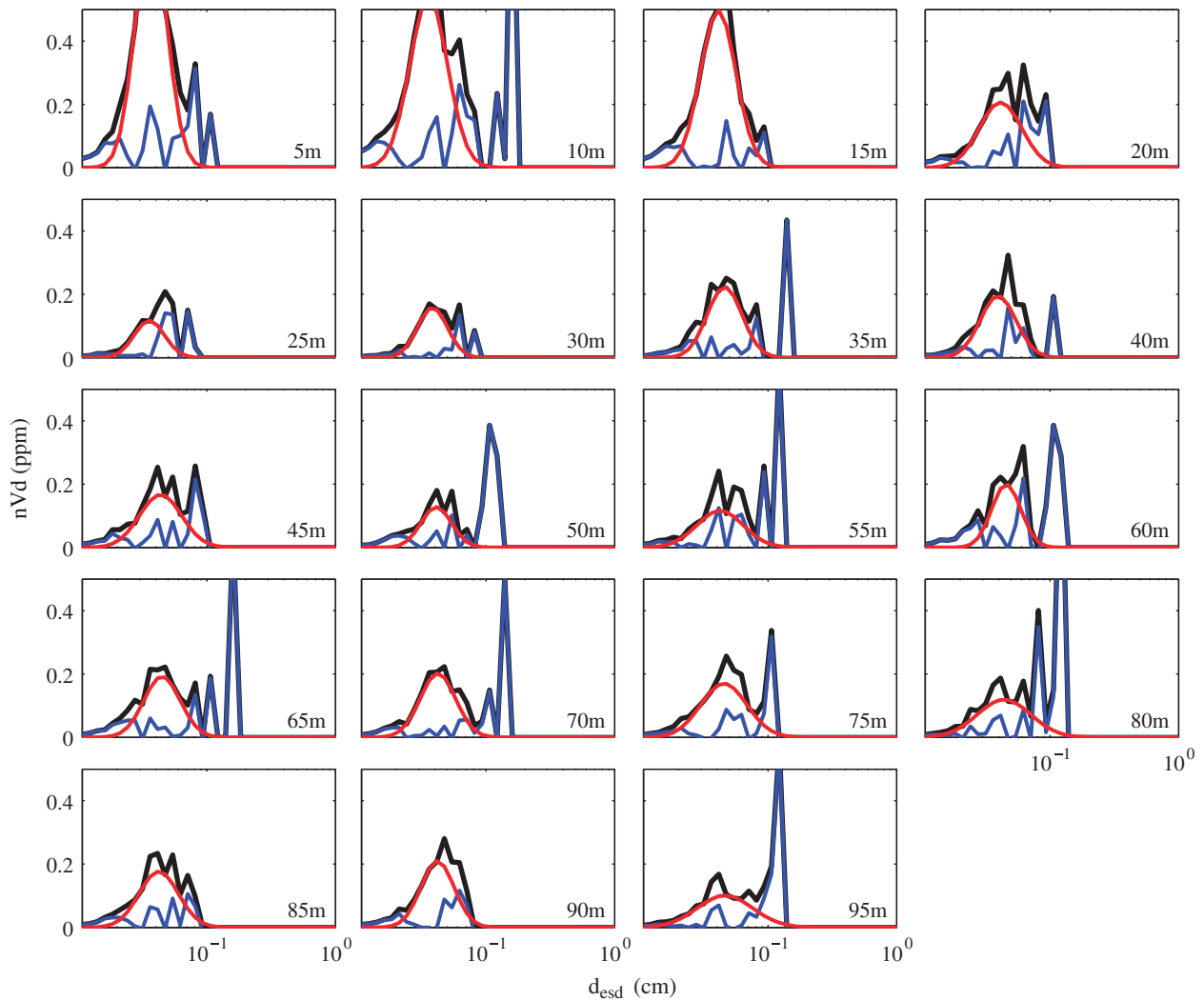


Fig. 4. Example of the normalized volume spectra, $n_{tot} Vd$ (black), their y_g fits (red (light gray)), and the residual ($n_{tot} Vd - y_g$; blue (dark grey)) from one profile (dive 4) during GK10_2.

Table 3

Correlation coefficients (r) for the Gaussian volume (V_{agg}), residual volume (V_{res}), and particulate organic carbon (POC) concentration with the volumes of different measures of particles: all particles (V_{tot}), *sno*-particles (V_{sno}), and *zoo*-particles (V_{zoo}), from all deployment samples grouped together. In addition, correlations of V_{agg} and V_{res} with fluorescence were calculated for Gatekeeper (FI GK) and non-Gatekeeper (FI nonGK) deployments. In parentheses are the number of data points.

Variable	V_{agg}	V_{res}	POC
V_{tot} (13,889)	0.43	0.99	0.27
V_{sno} (13,889)	0.85	0.55	
V_{zoo} (13,889)	0.34	0.99	
V_{agg} (13,889)	–	0.36	0.39
V_{res} (13,889)	0.36	–	0.18
POC (44)	0.39	0.18	–
FI GK (6175)	0.58	0.01	
FI nonGK (6327)	0.63	0.20	

V_{zoo} for the different deployments were much smaller, with r ranging from 0.01 to 0.75, and a mean of 0.20 (Table 4).

V_{res} correlated very highly with V_{zoo} , having r ranging from 0.93 to 1.0 for individual deployments (Table 4) and $r = 0.99$ for

Table 4

Correlation coefficients (r) between V_{agg} and different particle measures for separate deployments: raw fluorescence (FI), all particles (V_{tot}), *sno*-particles (V_{sno}), *zoo*-particles (V_{zoo}), and residual particles (V_{res}); correlation coefficients (r) between V_{res} and V_{zoo} for each deployment. In parentheses next to each deployment are the number of data points.

Deployment (n)	V_{agg}					V_{res}	
	FI	V_{tot}	V_{sno}	V_{zoo}	V_{res}	FI	V_{zoo}
SP05 (1197)	–	0.19	0.60	0.04	0.07	–	0.96
NH06 (1634)	0.79	0.54	0.92	0.21	0.20	0.07	0.99
SP07_1 (171)	0.80	0.31	0.82	0.01	0.16	0.14	0.97
SP07_2 (228)	0.78	0.04	0.63	–0.01	0.06	0.01	0.97
TH07_1 (1330)	0.79	0.30	0.87	0.14	0.17	0.23	0.99
TH07_2 (1364)	0.71	0.19	0.58	0.07	0.12	0.12	0.94
TH07_4 (1444)	0.67	0.24	0.55	0.06	0.06	0.02	0.98
BL08 (190)	–	0.78	0.85	0.15	0.36	–	0.93
GK10_1 (779)	0.17	0.07	0.29	0.05	0.02	0.11	0.95
GK10_2 (3648)	0.33	0.38	0.62	0.36	0.39	0.08	0.99
GK10_3 (589)	0.42	0.65	0.72	0.50	0.53	0.47	0.98
GK10_4 (152)	0.94	0.77	0.96	0.75	0.75	0.66	1.00
GK10_7 (1159)	0.57	0.31	0.85	0.23	0.25	0.12	0.97
Mean (13,889)	0.63	0.37	0.71	0.20	0.24	0.18	0.97
Median (13,889)	0.71	0.31	0.72	0.14	0.17	0.12	0.99

data from all deployments combined (Table 3). The correlation between V_{res} and sno -particle volume for the combined data ($r=0.55$; Table 3) was lower than the correlation with zoo -particle volume.

3.2.2. Comparisons between bottle and SOLOPC measurements

A linear regression between total chlorophyll concentrations measured on bottle samples and chlorophyll concentrations calculated from SOLOPC fluorescence from the GK10 deployments yielded

$$\text{Chl}_{\text{bottle}} (\mu\text{g L}^{-1}) = -0.0031 + 0.69 * \text{Chl}_{\text{SOLOPC}} (\mu\text{g L}^{-1}) \quad (9)$$

with a correlation coefficient $r=0.81$ with all data ($n=38$), and $r=0.91$ ($n=37$) and little change in the regression line when one outlier was dropped. That is, the values for chlorophyll concentrations in bottle samples were about two-thirds of those from the SOLOPC. This difference may be due, in part, to the SOLOPC sensing all in situ chlorophyll *a* while extracted chlorophyll was only from particles retained on the 1 μm filters. It may also reflect errors in instrument calibration or variability in the phytoplankton assemblage.

V_{agg} was strongly correlated with fluorescence for individual non-GK deployments, with $r=0.67$ – 0.80 (Table 4); the correlation decreased slightly when the data from the deployments were pooled together, $r=0.63$ (Table 3). The range of correlations was larger for the GK deployments ($r=0.17$ – 0.94 ; Table 4), but the correlation for the combined data was similar, $r=0.58$ (Table 3). Correlations between V_{res} and fluorescence from both non-GK and GK deployments were much smaller, $r=0.20$, 0.01 respectively (Table 3).

There were three deployments with nearly simultaneous collections of water samples for POC analyses (GK10_1, GK10_3, and GK10_7). The POC concentrations were more strongly correlated with V_{agg} ($r=0.39$) than with V_{tot} ($r=0.27$) or with V_{res} ($r=0.18$; Table 3). The mean $\text{POC}:V_{agg}$ was $56 \mu\text{g mm}^{-3}$; the values of $\text{POC}:V_{tot}$ and $\text{POC}:V_{res}$ were lower, 23 and $32 \mu\text{g mm}^{-3}$, respectively. The average $\text{POC}:V$ value for diatoms, $67 \mu\text{g mm}^{-3}$ (Mullin et al., 1966), is closest to that for $\text{POC}:V_{agg}$.

A multiple linear regression calculated using MATLAB *Linear-Model-fit* with $\text{POC} (\mu\text{g C L}^{-1})$ as the dependent variable, with $\text{Chl}_{\text{SOLOPC}} (\mu\text{g L}^{-1})$ and $V_{agg} (\text{mm}^3 \text{L}^{-1})$ as the independent variables, and removal of the same outlier as in Eq. (9) yielded

$$\text{POC} (\mu\text{g C L}^{-1}) = 72 + 23 (\pm 9, p = 0.017) * \text{Chl}_{\text{SOLOPC}} (\mu\text{g L}^{-1}) + 20 (\pm 19, p = 0.28) * V_{agg} (\text{mm}^3 \text{L}^{-1}) \quad (10)$$

where \pm indicates a standard error estimate. The coefficient for V_{agg} is essentially the same as the regression coefficient calculated above in the single regression. The relationship between Chl and POC is much tighter than between V_{agg} and POC .

3.2.3. Fractal dimension

The fractal dimension was remarkably constant over the deployments, with the mean $f=1.87$ (median $f=1.74$; Table 5). Note that the method for estimating f has improved since Jackson and Checkley (2011), so that the values are not necessarily the same as in that paper. There was only one value of f calculated per deployment, as the procedure used all the observations of a deployment. Fractal dimension increased with d_{μ} ($r=0.37$) and V_{agg} ($r=0.32$), indicating that bigger and possibly more numerous aggregates were less porous. These higher f values were derived from a narrower range of aggregate sizes, as f decreased with increasing σ ($r=-0.09$).

3.2.4. Estimated settling rates

Average settling velocities for a deployment estimated from the size distributions of the Gaussian fraction, \bar{v} , ranged from 20 to 65 m d^{-1} (Table 5). The mean of all deployments was 30 m d^{-1} (median = 27 m d^{-1}). The settling velocities estimated from cross-correlations between V_{agg} at different depths for varying time offsets, v_{xc} , were more variable, ranging from 13 to 383 m d^{-1} with a mean of 108 m d^{-1} and a median of 50 m d^{-1} (Table 5). The highest settling rate estimates were for GK10_4, which the high d_{μ} and f values indicate had larger, less porous particles than the other deployments (Table 5).

3.2.5. Identification of the Gaussian-fit (y_g) fraction with aggregates

Because of the relationships between the volume of y_g and multiple properties associated with aggregates, we will identify the Gaussian-fit fraction as aggregates for the rest of this paper (see Section 4.1.1).

3.3. Distribution of the particles and their properties

3.3.1. The Gatekeeper cruise deployment 2 (GK10_2)

Oceanographic properties. The Gatekeeper cruise sampled a region characterized by upwelling and relaxation in and around Monterey Bay, California. Deployments GK10_1, 3, 4, and 7 were launched in Monterey Bay, while GK10_2 was launched outside Monterey Bay. The GK10_2 deployment was the longest thus far of the SOLOPC, with 192 profiles spanning almost 210 h (Table 2). The resulting record of particle distributions provided a good data set to study changes in particle size distributions as functions of time and depth. The SOLOPC for GK10_2 was launched into what turned out to be a jet, and moved offshore from the upwelling region off Monterey Bay. On 18 July, it approached the California Current and turned south. The California Current influence can be seen in a layer of low salinity water between 30 and 70 m (Lynn and Simpson, 1987), particularly from 20–23 July (Fig. 5a). During this time, the mixed layer deepened (Fig. 5b) and the fluorescence decreased (Fig. 5c).

The lower surface temperature and shallow surface mixed layer in Monterey Bay indicate that upwelling was underway during the deployments. The cold water inshore was accompanied by high chlorophyll concentrations generally near the surface. There were high concentrations of particles, both zooplankton and aggregates, throughout the region, not just in Monterey Bay.

Table 5

Means of d_{μ} , σ , settling rates calculated using size distributions (\bar{v}) and cross-correlations (v_{xc}), and the fractal dimension (f) for each deployment.

Deployment	d_{μ} (cm)	σ (ln(cm))	V_{agg} (ppm)	\bar{v} (m d^{-1})	v_{xc} (m d^{-1})	f (–)
SP05	0.052	0.49	0.50	40	32	1.30
NH06	0.048	0.54	1.09	37	107	1.51
SP07_1	0.039	0.43	0.26	24	22	1.44 ^a
SP07_2	0.041	0.42	0.23	25	30	3.73 ^a
TH07_1	0.042	0.52	1.68	30	376	1.80
TH07_2	0.038	0.44	0.19	23	383	1.40
TH07_4	0.044	0.52	0.60	32	30	1.67
BL08	0.038	0.44	1.51	24	86	1.74 ^a
GK10_1	0.039	0.38	0.29	22	28	1.71
GK10_2	0.044	0.37	0.25	27	13	1.77
GK10_3	0.043	0.40	0.71	27	50	1.93
GK10_4	0.062	0.55	2.63	54	175	2.07 ^a
GK10_7	0.046	0.42	0.50	30	65	1.90
Mean	0.044	0.46	0.80	30	108	1.87
Median	0.043	0.44	0.50	27	50	1.74

^a Indicates fewer than 15 total data points for estimation of f , leading to questionable separation of sno - and zoo -particles.

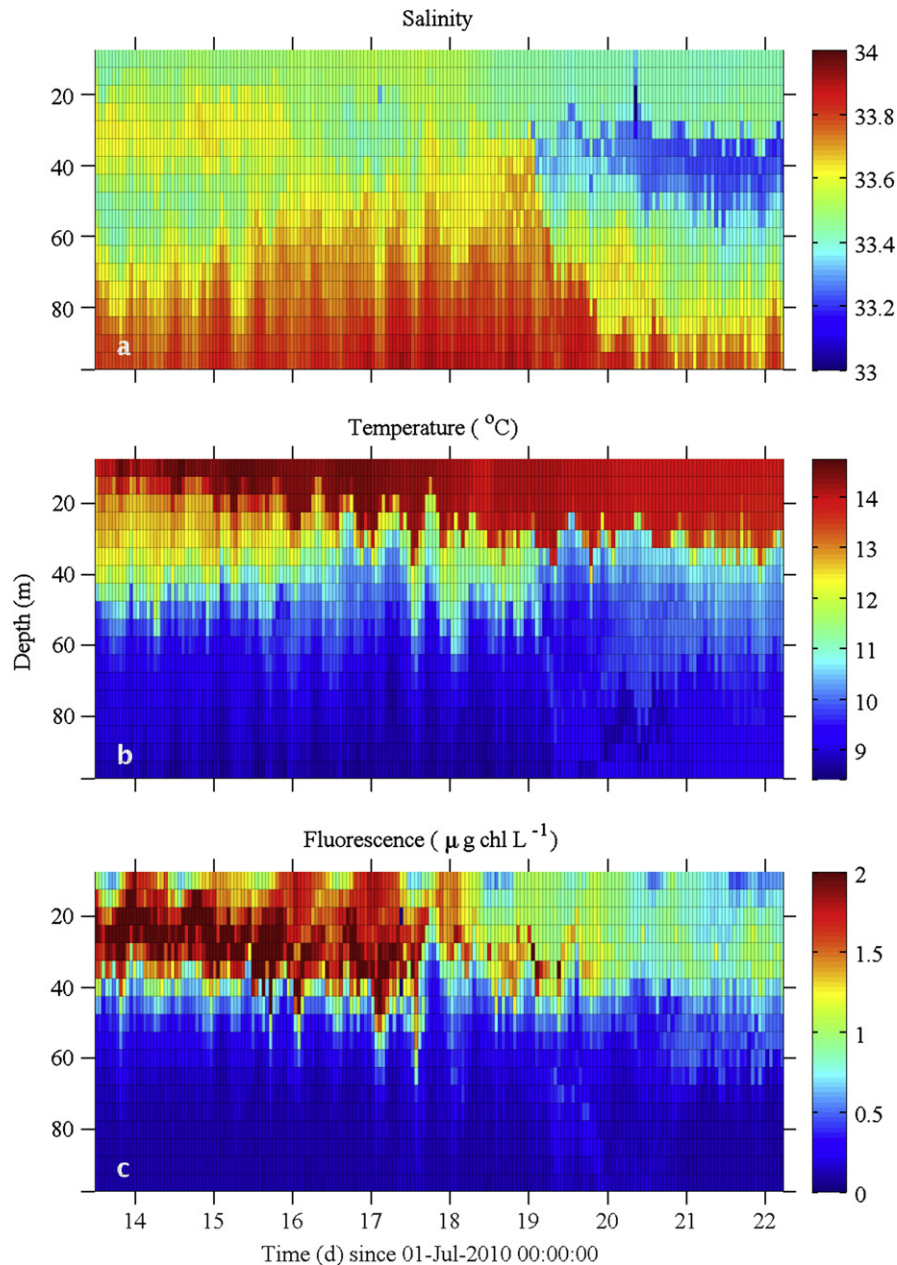


Fig. 5. Spatial distribution of (a) salinity, (b) temperature ($^{\circ}\text{C}$), and (c) fluorescence ($\mu\text{g chl L}^{-1}$) for all dives of the GK10_2 deployment.

Particle concentrations. There were consistently high particle concentrations near 30 m in the offshore deployment GK10_2 (Fig. 6a). The total particle volume for the deployment increased greatly once the SOLOPC float neared the California Current, with the maximum value of V_{tot} in the upper 100 m going from about 0.7 ppm at the beginning to as large as 255 ppm at the end of the deployment. (Note that the scales in Fig. 6 are set well below this maximum to show variations at lower concentrations.) The high values of V_{tot} were between 40 m depth and the surface, localized within a band 5–15 m thick, and appear to have varied with a diel periodicity. For the last four days of the deployment, the maximum was shallowest in the last quarter of the day, just after dusk. There was also evidence in the distributions of a downward movement of material on 19, 20, and 21 July.

The residual fraction, V_{res} , had similar concentrations and cycles as V_{tot} (Fig. 6b). Not surprising, this included the near-surface diel cycling at the end of the deployment. The volumes of residual particles were generally larger than the associated values

of V_{agg} and accounted for most of V_{tot} (Fig. 6a, b). The depth maximum of V_{res} was between 20 and 40 m and suggested a different diel pattern (Fig. 6b). The removal of the aggregate distribution from the total particle $n_{tot}Vd$ removed most of the downward movement of material.

The aggregate fraction was smaller in volume than V_{tot} and V_{res} , typically less than 1 ppm (Fig. 6c). Before 17 July, the smallest aggregates were in the surface waters; afterwards there was a band of small particles around 30 m (Fig. 7), which was also the depth of the greatest volume of aggregates. Most of the diel variability seen in V_{tot} during the last three days of the deployment is absent from the aggregate record (Fig. 6a, c). However, the downward movement of material is present and more prominent.

A comparison of the mean distributions of volume for the different fractions shows that the average value of V_{tot} peaked at 17.5 m with a value of almost 8 ppm (Fig. 8); the average value of V_{res} also peaked there at about 7.5 ppm. The maximum

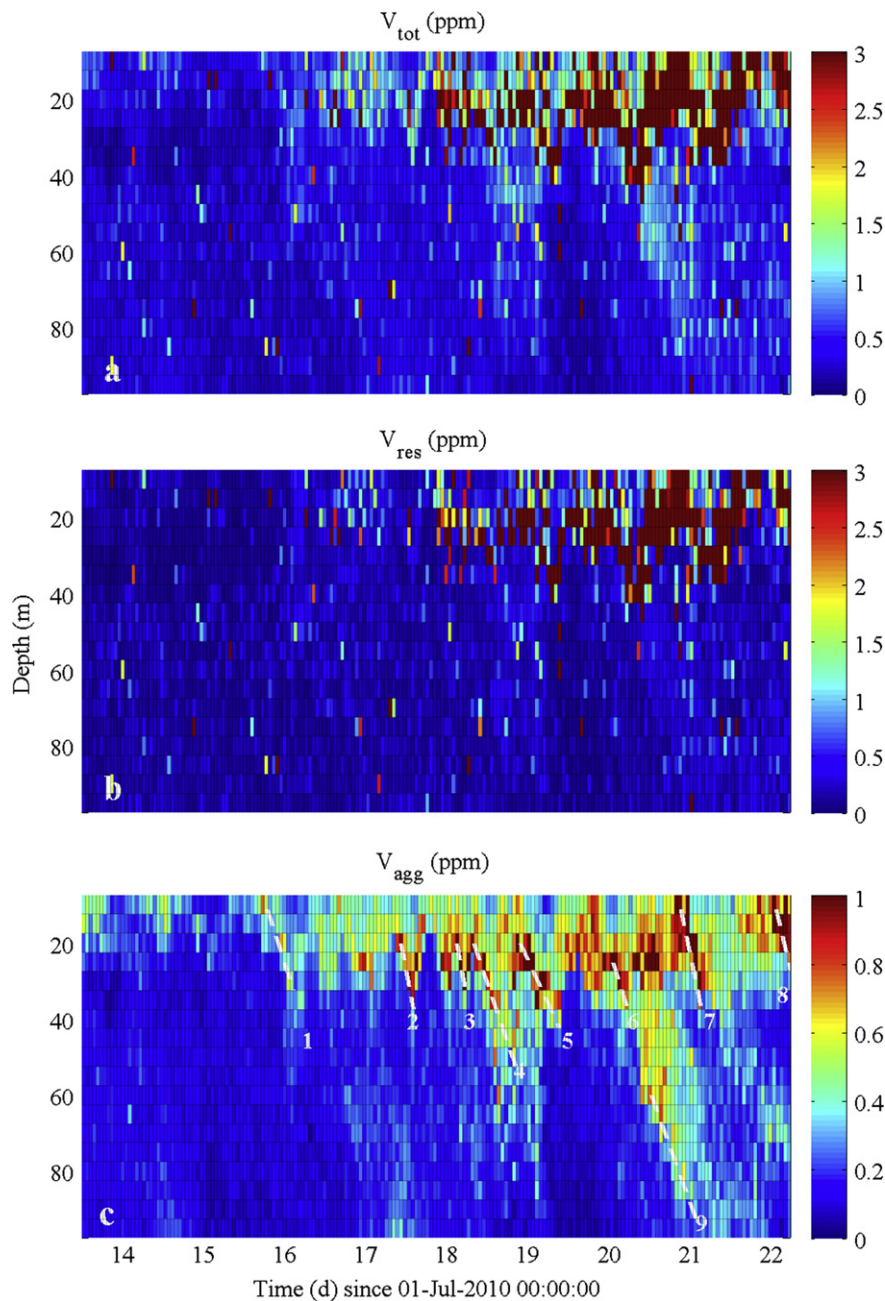


Fig. 6. Depth and time variation in the volumes of (a) all particles (V_{tot}), (b) the residual (V_{res}), and (c) the aggregate fraction (V_{agg}) for all dives of deployment GK10_2. The colorbar scales were chosen for viewing ease, but outliers extended above them (maximum $V_{\text{tot}} = 255$, $V_{\text{res}} = 254$, $V_{\text{agg}} = 2$). Sinking trajectories (white dotted lines) are superimposed on V_{agg} in (c).

concentration value of V_{agg} was about 0.5 ppm at that depth, but it was not as sharp as the other two maxima. Below 40 m, the average concentrations of V_{res} and V_{agg} were almost the same, although V_{res} tended to be slightly larger. The median diameter (d_{μ}), distribution width (σ), and volume (V_{agg}) of the aggregates increased near the California Current (Figs. 6 and 7).

Sinking particles. To investigate the sinking events, evidenced by the downward propagation of particles similar in size and volume, we subjectively chose seven of the prominent events (Fig. 6c, white lines) and calculated the changes in aggregate volume and median diameter along them, starting near the depth of maximum V_{agg} . Since these trajectories were started at what appeared to be the highest volumes, volume decreased along them (Fig. 9a). Size tended to decrease along the sinking trajectories as well (Fig. 9b). Sinking rates calculated from these

trajectories ranged from 45 to 108 m d^{-1} with a mean of 82 m d^{-1} (median = 86 m d^{-1} ; Table 6).

The relative rate of decrease in particle volume along the path can be related to grazing pressure, either by flux feeding or filter feeding (e.g., Stemmann et al., 2004a; Iversen et al., 2010). The mean fractional change in volume with depth along a trajectory ($V_{\text{agg}}^{-1} dV_{\text{agg}}/dz$) can be used to compare against potential flux feeding rates and was negative for all trajectories, indicating continual net losses along the path. Its mean value for all trajectories was -0.035 m^{-1} (median = -0.040 m^{-1} ; Table 6). This would be equivalent to a mean particle collection area of flux feeders equal to $350 \text{ cm}^2 \text{ m}^{-3}$. If the dominant loss was from filter feeding organisms instead, the fractional decrease with time along the path is the useful metric of comparison. Its mean value over all trajectories, also negative for all, was -2.93 d^{-1}

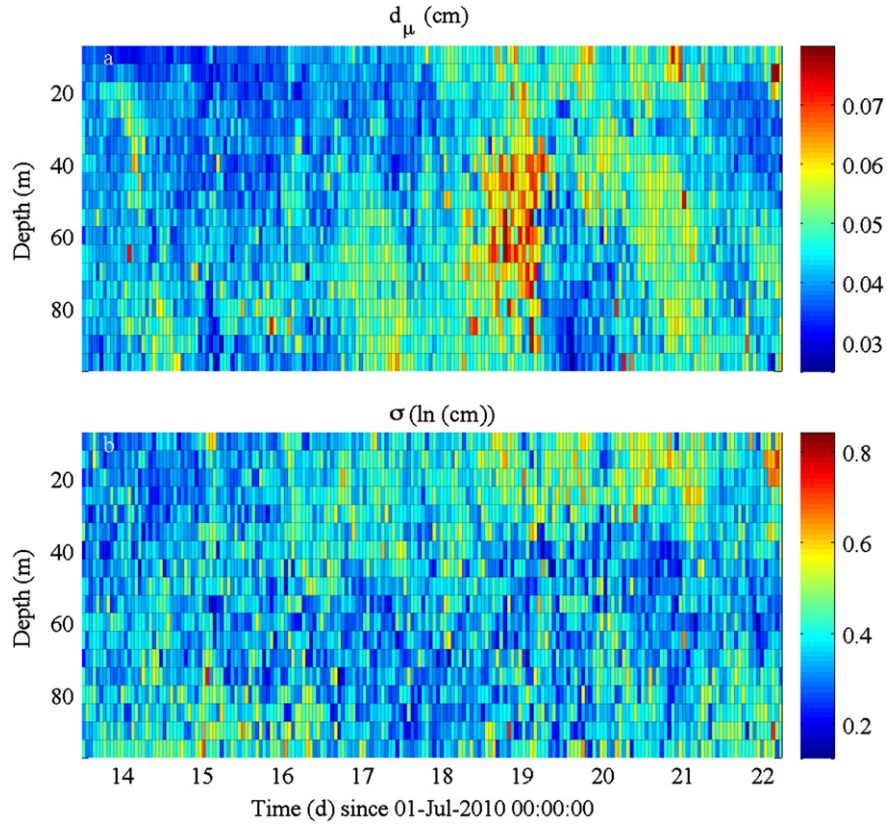


Fig. 7. Depth and time variation in (a) d_μ and (b) σ for all dives of deployment GK10_2.

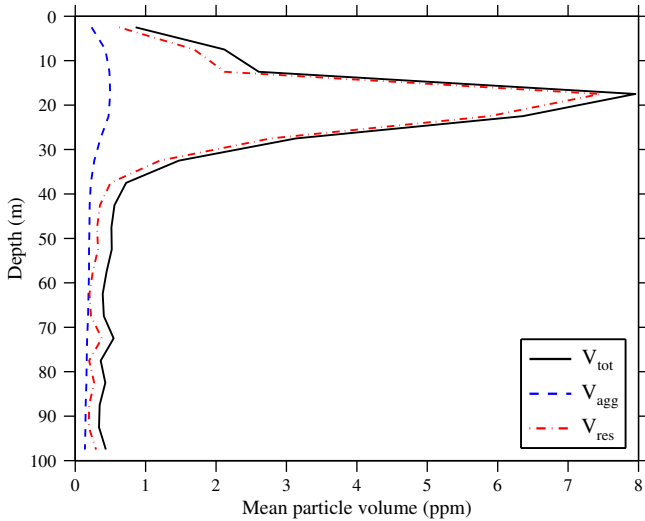


Fig. 8. Mean particle volume for different particle fractions as a function of depth during GK10_2.

(median = -2.32 d^{-1} ; Table 6). If the losses were from filter feeding, this would be equivalent to a mean filtration rate of $2.93 \text{ m}^3 \text{ d}^{-1}$ per m^3 . If the volume losses were actually shrinkage caused by microbial degradation or animal mining, the fractional change in median diameter with depth ($d_\mu^{-1} dd_\mu/dz$) and time ($d_\mu^{-1} dd_\mu/dt$) are the useful metrics and should be negative to signify shrinkage. Their values were negative for 4 of the 7 trajectories, with the depth decrease having a mean value of -0.002 m^{-1} (median = -0.006 m^{-1}) and the mean time decrease being -0.41 d^{-1} (median = -2.32 d^{-1} and -0.65 d^{-1} ; Table 6).

3.3.2. All deployments

The mean depth profiles of the Gaussian fit parameters differed among deployments, with values of d_μ ranging from 0.033 to 0.086 cm, σ between 0.34 and 0.66, and V_{agg} between 0.07 and 10.36 ppm (Fig. 10). Values of d_μ were relatively constant with depth for GK10_2 (Fig. 10a), but increased with depth for NH06 and TH07_1 (Fig. 10b). Conversely, most deployments (SP07_1, SP07_2, TH07_2, TH07_4, GK10_1, GK10_3, GK10_4, GK10_7) had maxima between the surface and 100 m (Fig. 10a, b). Depths of this subsurface maximum varied between 30 and 70 m. The smallest d_μ values occurred in TH07_2, while the largest in GK10_4 (Table 5). Values of σ tended to be largest in the upper or mid water column and smallest deeper (Fig. 10c, d). Most deployments had the largest mean aggregate volumes between 10 and 40 m (Fig. 10e, f). Exceptions were TH07_2, with its greatest value near 60 m, and GK10_4 and GK10_7, with maxima near the surface (Fig. 10e, f). The maximum mean V_{agg} of TH07_2 was the lowest of all deployments, while GK10_4 was the highest (Table 5).

There was no consistent pattern in the location of the depth of the fluorescence maximum relative to the maximum V_{agg} . The peak in fluorescence tended to be above the peak in V_{agg} for 6 deployments, at the same depth in 1, and below in 3 deployments (Table 7). There were no strong correlations between V_{agg} and N_{BV}^2 in any of the deployments ($-0.23 < r < 0.23$), with the exception of SP05 ($r=0.71$). The N_{BV}^2 maximum was below the V_{agg} maximum the majority of the time in 10 of the 13 deployments.

Diel patterns like those seen in GK10_2 can be seen in the depth-averaged values of V_{agg} and V_{res} in the longer deployments ($> 24 \text{ h}$). The average aggregate volume between 5 and 100 m had a maximum that occurred as early as 0900 and as late as 0100 h, but most often occurred during the afternoon. The minimum occurred at night, between 1800 and 0600 h (Table 7).

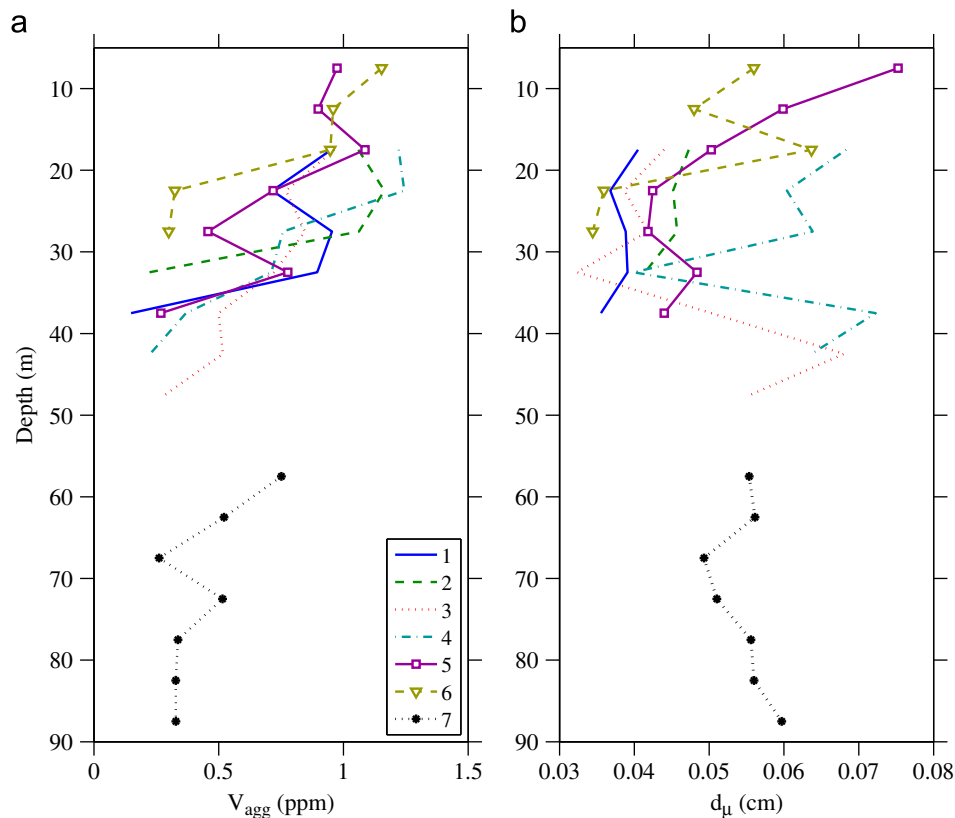


Fig. 9. Aggregate (a) volume (V_{agg}) and (b) median diameter (d_{μ}), with time along the GK10_2 sinking trajectories labeled in Fig. 6c.

Table 6
Sinking rate, fractional change of aggregate volume with depth, $V_{agg}^{-1}dV_{agg}/dz$, fractional change of aggregate median diameter with depth, $d_{\mu}^{-1}dd_{\mu}/dz$, fractional change of aggregate volume with time, $V_{agg}^{-1}dV_{agg}/dt$, fractional change of aggregate median diameter with time, $d_{\mu}^{-1}dd_{\mu}/dt$, along the 7 sinking trajectories labeled in GK10_2 (Fig. 6c).

Trajectory	Sinking rate ($m\ d^{-1}$)	$V_{agg}^{-1}dV_{agg}/dz$ (m^{-1})	$d_{\mu}^{-1}dd_{\mu}/dz$ (m^{-1})	$V_{agg}^{-1}dV_{agg}/dt$ (d^{-1})	$d_{\mu}^{-1}dd_{\mu}/dt$ (d^{-1})
1	107	−0.040	−0.006	−4.35	−0.65
2	108	−0.052	−0.008	−5.61	−0.91
3	62	−0.032	0.015	−2.02	0.95
4	45	−0.052	0.010	−2.32	0.46
5	106	−0.018	−0.016	−1.87	−1.66
6	86	−0.046	−0.015	−3.94	−1.26
7	57	−0.007	0.003	−0.39	0.17
Mean	82	−0.035	−0.002	−2.93	−0.41
Median	86	−0.040	−0.006	−2.32	−0.65

To investigate vertical migration of the zooplankton, we examined changes in a limited depth range by using the residual volume as our proxy and calculating the mean V_{res} over the 15 m near-surface depth range (5–20 m). The mean V_{res} had a maximum at similar afternoon times as mean V_{agg} , from 1100 to 1700 h with an outlier at 0100 (Table 7). The maximum mean V_{res} occurred after the maximum mean V_{agg} in 6, possibly 7 of the 9 longer deployments. The minimum in mean V_{res} was almost always in the morning between 0600 and 1000 h, with one occurrence at 2200 h (Table 7). These lows in mean V_{res} also tended to occur after those in V_{agg} .

Deployment TH07_4 provides an example of these diel patterns. The vertical mean V_{agg} was larger than the deployment mean during 1100–2000 h and smaller from 2200 to 0700 h

(Fig. 11a). Similarly, near-surface mean V_{res} was larger than the deployment mean from 1500 to 0200 and smaller than the deployment mean during 0300–1200 (Fig. 11b).

4. Discussion

4.1. The aggregate fraction

4.1.1. Identifying the Gaussian fit as the aggregate fraction

Jackson and Checkley (2011) analyzed the pre-Gatekeeper cruise MEP data, associating the *sno*-particles with aggregates and the *zoo*-particles with zooplankton. In this paper, we extend the separation of the two particle types into the realm of the smaller SEPs.

The *sno*-particles, which only include MEPs ($d_{od} > 2\text{ mm}$), contribute a significant portion to the Gaussian fits (Fig. 12). We hypothesize that the difference between the Gaussian fraction and *sno*-particles is made primarily of aggregates with widths (d_{od} 's) $\leq 2\text{ mm}$. The *sno*-particles have the characteristics of aggregates, particularly their fractal dimensions. Excluding deployments with too few dives, values of f estimated for the *sno*-particles ranged from 1.30 to 1.80 for the pre-Gatekeeper cruises (1.30 to 2.09 in Jackson and Checkley, 2011) and 1.71 to 1.93 for Gatekeeper (Table 5), with an overall mean of 1.87 (Table 5). Previous estimates made by a variety of techniques range from 1.28 to 2.46 (e.g., Logan and Wilkinson, 1990; Kilps et al., 1994; Jackson et al., 1995, 1997; Guidi et al., 2008). The high correlations of V_{agg} with V_{sno} (mean of 0.71; Table 4) and low correlations with V_{zoo} support the idea that V_{agg} and V_{sno} are associated with the same fraction and that the Gaussian fitting procedure is isolating the aggregate fraction. The correlations between V_{agg} and V_{sno} are higher than correlations between total volume of the SEP fraction and V_{sno} for the same pre-Gatekeeper

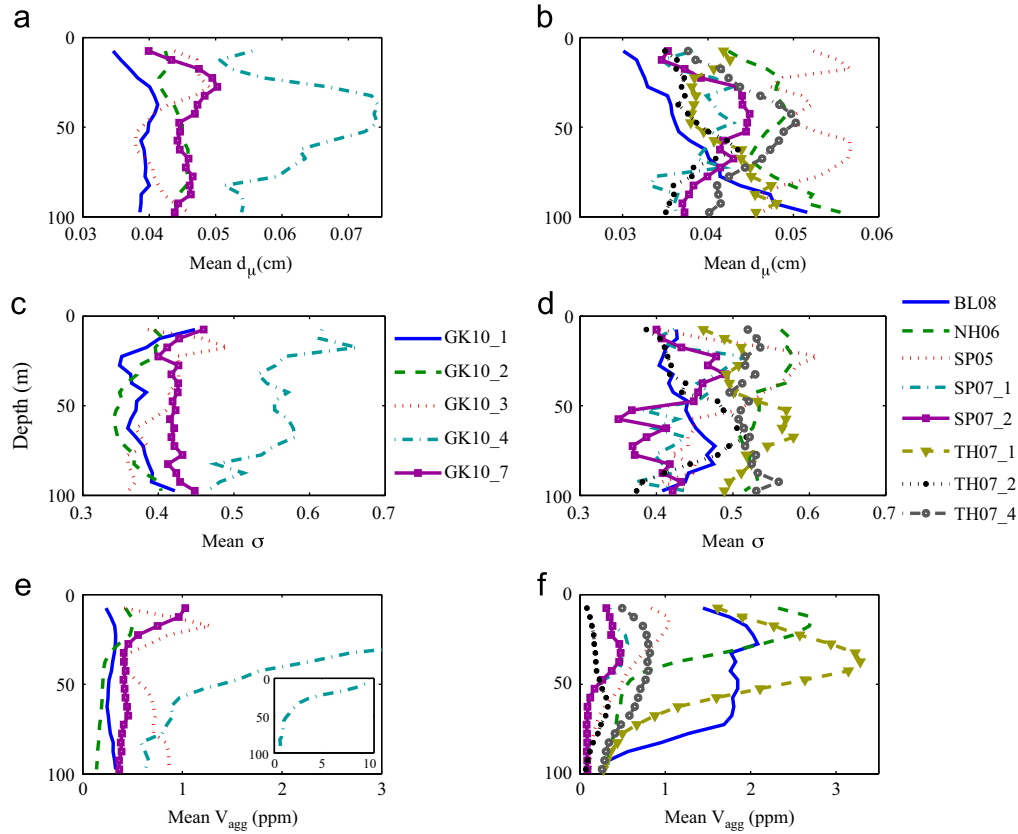


Fig. 10. Vertical distributions of mean (a, b) d_{μ} , (c, d) σ , and (e, f) V_{agg} for GK (a, c, e) and non-GK (b, d, f) deployments. The inset in (e) shows the full range of GK10_4.

Table 7

Deployment properties. Left: depth of maximum fluorescence and N_{BV}^2 relative to depth of maximum V_{agg} . Values indicate the number of profiles where the maximum property value was shallower, the same, or deeper than the maximum depth for V_{agg} . – indicates that no fluorescence measurements were taken. Right: Times (local hour of day) of the maximum and minimum V_{agg} and V_{res} for deployments longer than 24 h. Maxima and minima were found for the V_{agg} averaged over 5–100 m and V_{res} averaged over 5–20 m. – indicates that deployment was less than 24 h.

Deployment	Comparison with V_{agg}						Times for			
	Fluorescence			N_{BV}^2			Max.		Min.	
	Shal.	Same	Deep.	Shal.	Same	Deep.	V_{agg}	V_{res}	V_{agg}	V_{res}
SP05	–	–	–	13	17	33	13	17	5	9
NH06	37	30	19	2	2	82	9	17	22	8
SP07_1	3	3	3	1	1	7	–	–	–	–
SP07_2	1	6	5	4	1	7	–	–	–	–
TH07_1	50	13	7	42	1	27	12	14	20	8
TH07_2	5	23	44	3	7	62	13	17	18	10
TH07_4	48	8	20	10	5	61	–	–	–	–
BL08	–	–	–	3	0	7	–	–	–	–
GK10_1	24	8	9	31	4	6	19	12	3	22
GK10_2	10	25	157	20	42	130	1	11	6	6
GK10_3	14	14	3	25	2	4	10	17	6	9
GK10_4	2	2	4	0	0	8	–	–	–	–
GK10_7	29	29	3	21	9	31	16	12	1	9

cruises (Jackson and Checkley, 2011), suggesting that the Gaussian fitting procedure isolates the smaller particles most similar to the aggregate-like *sno*-particles. The Gaussian fitting procedure is better at separating aggregates and zooplankton, as correlations between V_{agg} and fluorescence are higher than between V_{sno} and fluorescence, while correlations between V_{agg} and V_{zoo} are lower than between V_{sno} and V_{zoo} (Jackson and Checkley, 2011).

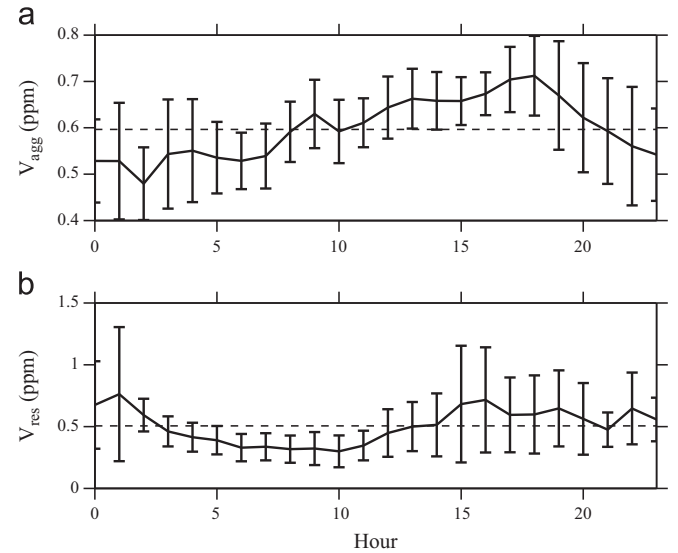


Fig. 11. Standardized mean volume vs. local hour for deployment TH07_4. (a) V_{agg} was averaged over 5–100 m. (b) V_{res} was averaged over 5–20 m. The dashed lines are the means of all hours.

We argue that the Gaussian fraction represents aggregates because it shares many of the important characteristics observed in marine snow and other marine aggregates. It has high correlations with fluorescence, POC, and transparent particles (*sno*-particles), and the POC:volume ratio of the Gaussian fraction is similar to Mullin et al. (1966) value for diatoms (Tables 3 and 4). Marine algae, particularly diatoms, are some of the most important sources of aggregates (Alldredge and Silver, 1988; Kranck and Milligan, 1988). The relationships between V_{agg} and the different

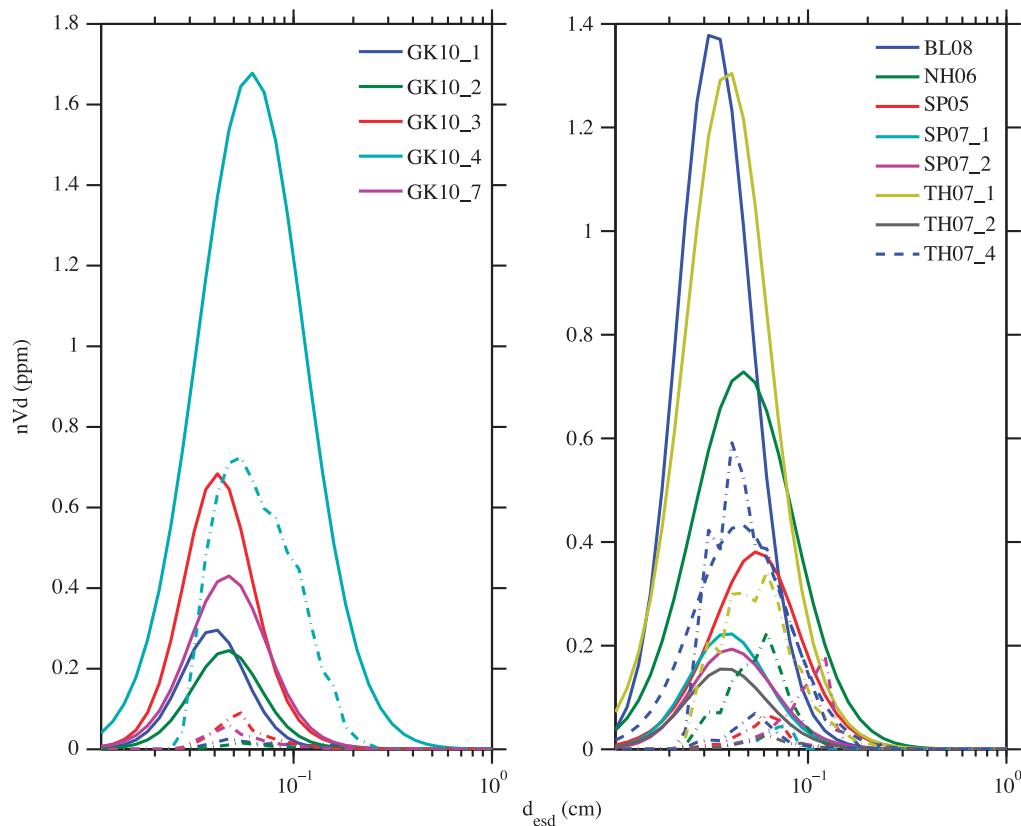


Fig. 12. Mean normalized volume spectra of aggregates, $n_{agg}Vd$, (black (solid lines in web version)) and *sno*-particles (gray (dashed lines in web version)) from all deployments.

algal-related properties support the identification of particles in the fraction identified by the Gaussian fitting procedure as aggregates.

Reported values of settling rates for marine snow particles span a large range, 1–368 m d⁻¹ (e.g., Stemann et al., 2004a), as they were estimated from many different sizes of aggregates using different methods. Our settling rates calculated from particle size distributions of each deployment (\bar{v}) and depth correlations of aggregate volume (v_{xc}) easily fall within this range, although v_{xc} of TH07_1 and TH07_2 are on the outer edge (Table 5). The similarity in settling rates further supports the identification of the Gaussian fraction as aggregates.

Interpreting the meaning of size for an aggregate estimated by any technique is difficult because of the extremely heterogeneous nature of particles, which can include algal cells, fecal pellets, animal molts, TEP, and water packaged in an irregular shape (e.g., Jackson et al., 1997). Some particle sizing techniques, such as the aperture impedance measurement used by the Coulter Counter, estimate a property approximately equal to the volume of an aggregate's solid fraction; other techniques return the size of an ellipse which surrounds a two dimensional image of an aggregate, solid fraction plus contained water. Fractal scaling has been used to relate different measures (e.g., Jackson et al., 1995, 1997). In this LOPC case, the diameter estimated from light absorption (d_{esd}) is considered to be more like that of a sphere whose volume is proportional to its mass. Such an interpretation is consistent with the fact that the d_{esd} is related to its maximal extent, the d_{od} , with fractal dimensions of about 1.8. This is similar to the fractal dimension used to relate masses and lengths for aggregates collected in the field (Kilps et al., 1994).

Thus, all the properties that we are able to use support the idea that the Gaussian fitting procedure isolates the aggregate fraction in the particle pool. However, it must be stated that this is an

empirical fitting procedure that could capture microzooplankton as well as aggregates. The differences between the $n_{tot}Vd$ and its Gaussian fit, the residual, are hypothesized to be small zooplankton, such as forams and radiolarians, which are in the aggregate size range. In fact, they might be part of the Gaussian peak. This hypothesis will be examined in the future with observations from concurrent net tows.

The relationship between the Gaussian fit and aggregates will need to be tested in different systems and with other particle measurement techniques, as well as by modeling efforts. The fact that the correlations between V_{agg} and other aggregate surrogates were similar in the phytoplankton-rich Monterey Bay region (GK_3-7) and in the oligotrophic side of the California Current (TH07_2) suggests that the association is not limited to algal aggregates. In fact, the correlation between V_{agg} and fluorescence was least for the GK_2 cruise that showed characteristic aggregate sinking behavior, suggesting that this will prove to be a robust technique.

There is no doubt that the more properties of particles we are able to measure, the better our understanding of the particles. We are exploring the comparison of these results with observations of zooplankton species and abundances made with plankton nets and with image-based particle sizing. Comparing results from different techniques is complicated by the fact that all measure different physical properties that do not easily relate to each other. However, it is important that we be able to do this if we are to understand animals and aggregates in the plankton.

4.1.2. Simulations of aggregate formation

Simulations of aggregation by exponentially growing single cells yield nVd distributions that are skewed to single cells. However, simulations in which there is also growth in chains or

disaggregation do yield lognormal distributions. In addition, one-dimensional simulations yield such distributions below the euphotic zone, when source particles no longer dominate (Jackson, unpublished results). Better parameterization of coagulation models may produce a closer fit with observations.

To the extent that aggregates are being formed by coagulation of algal cells, there should be a relationship between the concentrations of the two (e.g., Jackson, 1990). Because the rate of collisions between two algae is proportional to the square of the algal concentration, the rate of aggregate formation should be a non-linear function of algal concentration, while settling losses of similar sized aggregates should be linearly proportional to aggregate concentration. Sinking can also affect the relative concentrations of phytoplankton and aggregates. For example, if solitary algal cells fall slower than aggregates, the relative concentration of aggregates could increase with depth. Lastly, the spatial structure of consumption by grazers or bacteria can also affect their relative concentrations (e.g., Jackson and Checkley, 2011).

A comparison of estimated aggregate and phytoplankton carbon concentrations, using the regression coefficients in Eq. (10) to normalize the two quantities to the same carbon concentration units, shows interesting patterns. The three deployments in the upwelling area off Point Conception (NH06, TH07_1, and TH07_4) had greater aggregate concentrations, particularly at low algal concentrations, deeper in the water column (Fig. 13). There was also a general pattern of greater aggregate concentrations at larger algal concentrations, which is consistent with algae producing them. In contrast, the oligotrophic TH07_2 had relatively greater plant concentrations, again consistent with lower aggregate production.

For most of the Gatekeeper deployments, the plant concentrations tended to be greater and there was little relationship with aggregate concentration. The clear exception was GK10_4, where

aggregate and plant concentrations were the highest observed and where the two increased together.

The differences between the regions may indicate that other factors are also important in the formation of aggregates. These could include differences in the production and concentrations of exopolymeric materials, such as TEP, and the different algal species with different tendencies to aggregate because of stickiness or chain formation (e.g., Kiørboe et al., 1990; Logan et al., 1995; Engel, 2000). There is no reason to believe that the C:volume and C:chl ratios were constant in the different deployments. However, using the values calculated during the Gatekeeper cruise does provide a common scale to compare plant and aggregate concentrations.

4.1.3. Distribution of the aggregate fraction

Larger mean values of σ in the upper and mid water column indicate that the aggregate size range was greater at these depths (Fig. 10c, d). Most deployments featured subsurface maxima of d_{μ} and V_{agg} (Fig. 10a, b, e, f). Aggregate sizes were largest between 30 and 70 m (Fig. 10a, b), whereas volumes were greatest at shallower depths between 10 and 40 m (Fig. 10e, f). The median diameter of aggregates in 10 of the 13 deployments decreased below 60 m. This pattern is different than that noted in passing by Lampitt et al. (1993b), but their observations extended much deeper than ours, to 300 m, and may not be strictly comparable. It is also different than the pattern of increasing particle diameter for all particles, zooplankton and aggregates, reported by Jackson and Checkley (2011). Such a difference between the mean diameters for the two different particle groupings can be attributed to zooplankton distributions, as seen in their distributions of V_{sno} and V_{zoo} with depth (Jackson and Checkley, 2011). For example, deployment BL08 had a maximum in V_{agg} near 25 m

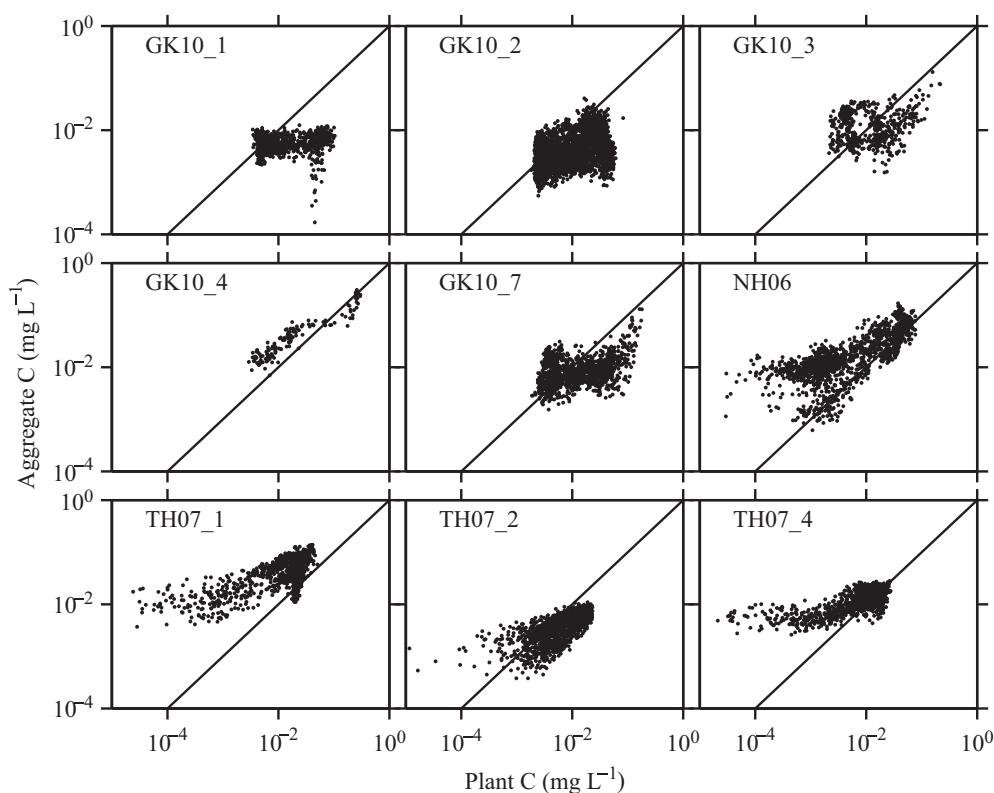


Fig. 13. Relationship between aggregate and phytoplankton carbon concentrations. These were calculated from V_{agg} and SOLOPC measurements of fluorescence, using relationships to C in Eq. (10). Each panel has data from one deployment, as indicated. The diagonal lines denote a 1:1 relationship.

(Fig. 10) that was not seen in V_{tot} , V_{sep} , or V_{sno} distributions (Jackson and Checkley, 2011).

Lampitt et al. (1993b) found peak concentrations of marine snow at the base of or just below the upper mixed layer, underneath the maxima in fluorescence or attenuation. MacIntyre et al. (1995) similarly observed peaks in aggregates near the pycnocline with maximum abundances at depths of maximum N_{BV}^2 , and the maximum volumes about 10 m below that. The GK10_2 maximum aggregate volumes near the California Current were also near the base of the mixed layer (Figs. 5 and 6c), but tended to be shallower than those in fluorescence (Table 7). The same pattern emerged in all the deployments: maximum V_{agg} was below the maximum fluorescence in 31%, at the same depth in 22%, and above in 47% of the dives (Table 7). This was different from the relationship between V_{tot} and fluorescence reported by Jackson and Checkley (2011), in which the maximum V_{tot} was shallower than the maximum fluorescence for only 15% of the dives. The deployments where peak fluorescence was generally shallower than peak V_{agg} (NH06, TH07_1, TH07_4, GK10_1) or where it was above and at the same depth an equal number of times (GK10_3, GK10_4, GK10_7) were all upwelling regions.

MacIntyre et al. (1995) suggested that smaller, less porous aggregates may accumulate at density interfaces as a result of turbulent mixing. However, Jackson and Checkley (2011) found

no evidence of this in the pre-Gatekeeper cruises when using V_{sno} as the aggregate measure. Our conclusions made comparing V_{agg} and N_{BV}^2 , rather than V_{sno} and N_{BV}^2 , are the same, as the maximum V_{agg} also tended to be above the maximum N_{BV}^2 (Table 7).

Alternately, downwelling at fronts could be responsible for aggregate accumulation and export (Gorsky et al., 2002; Stemmann et al., 2008). If this were the case, volume isolines would be parallel to isopycnals. Sinking events were present in GK10_2 (Fig. 14a), but were not restricted to this deployment as they were observed in others, such as TH07_1 in an upwelling region off Point Conception (Fig. 14b). In both deployments, aggregate volumes crossed density isopycnals (Fig. 14), which did not show evidence of any strong fronts. These results and the previous ones suggest that the mechanism responsible for the peak in aggregate volume was not related to downwelling fronts nor turbulence at density interfaces, and was distinct from that responsible for fluorescence.

The sharp decreases with depth in V_{agg} were similar to previous observations and estimates of particle concentrations, volumes, and fluxes, many of which were attributed to zooplankton feeding (Lampitt et al., 1993b; Stemmann et al., 2004b; Iversen et al., 2010; Jackson and Checkley, 2011). The GK10_2 sinking events and their corresponding decreases in V_{agg} appear to be diel, with the highest particle concentrations found at ~ 20 m

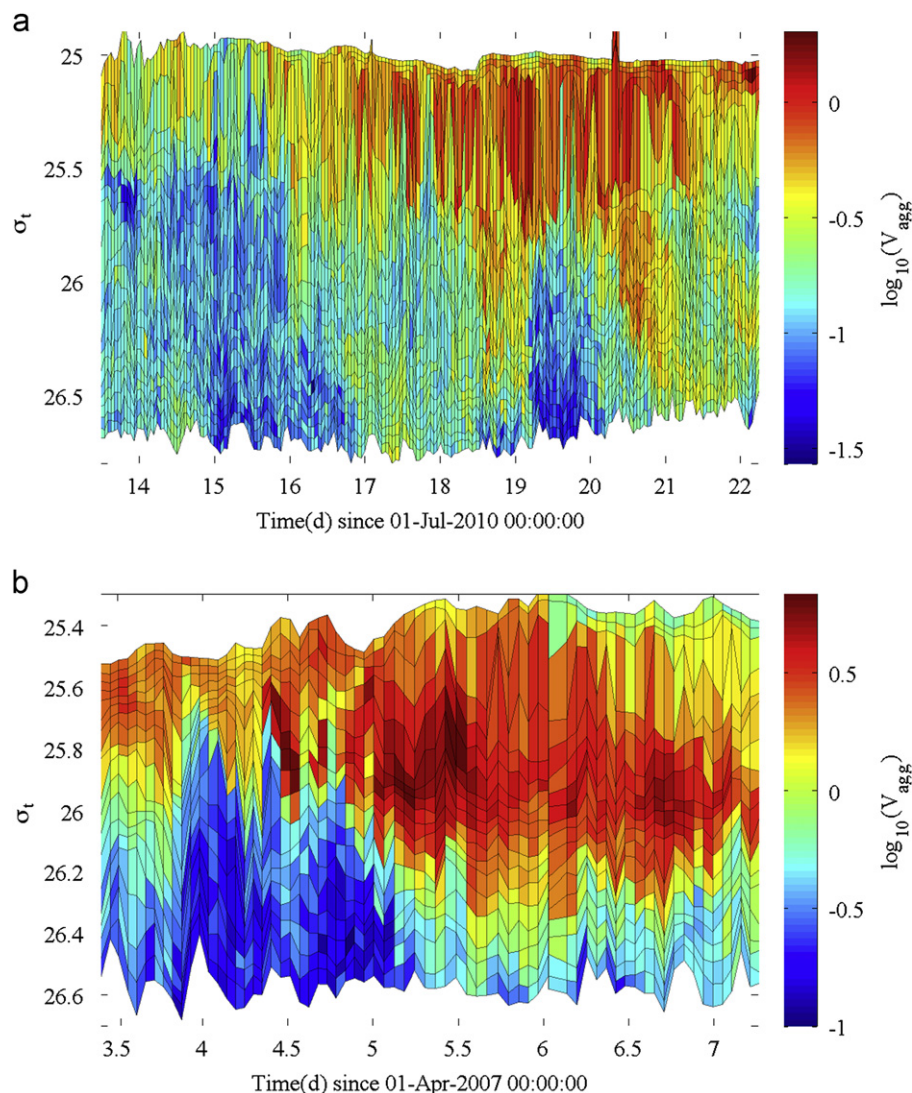


Fig. 14. Time series of \log_{10} aggregate volume (ppm), V_{agg} , with respect to density, σ_t (kg m^{-3}), from deployments (a) GK10_2 and (b) TH07_1.

depth near 0100 h (Fig. 6c). The other deployments also had diel patterns of V_{agg} with maxima in the afternoon and minima in the nighttime hours (Table 7). The maximum and minimum V_{agg} occurred at the same time as the maximum and minimum V_{sno} for TH07_4 (Jackson and Checkley, 2011), but the combined times of all deployments were earlier than those.

Diel cycles in integrated particle load, with evening highs and morning lows, have been reported by Walsh et al. (1995), Bishop and Wood (2008), Checkley et al. (2008), and Jackson and Checkley (2011), a pattern hypothesized to result from the balance of primary production and grazing. Conversely, Lampitt et al. (1993a) observed a daily cycle in aggregate concentration and volume at 270 m that was higher during the day than the night. Ruiz (1997) studied the mechanism for generating daily cycles of marine snow using a model and did not find marine snow cycles generated by cyclical grazing. Instead, Ruiz found that daily cycles of turbulence and solar radiation could cause cycles in aggregate number, mass, and transport down to a depth of 270 m with increased turbulence at night decreasing aggregations by fragmentation (Ruiz, 1997). We observed maximum aggregate volumes in the afternoon, followed by maximum residual volumes in the upper 5–20 m (see Section 4.2.2), and aggregate volume minima in the early morning (Table 7). These patterns are more consistent with zooplankton migration into the depths containing aggregates, reduction of the volume of aggregates by zooplankton feeding, and formation of new aggregates the following day.

4.2. The residual fraction

4.2.1. Associating zooplankton with the residual

In Jackson and Checkley (2011), the zoo-particle fraction was associated with zooplankton. Again extending the particle separations into the SEP size range, if the y_g fraction represents aggregates, then the residual should represent zooplankton. Such an association is consistent with the high correlations between V_{res} and the large, opaque zoo-particles, low correlations with fluorescence, POC, and *sno*-particles, and a POC:V ratio dissimilar from Mullin et al. (1966) value for diatoms (Tables 3 and 4). Furthermore, V_{res} in GK10_2 did not exhibit the same downward sinking that the aggregate fraction did. We will refer to this fraction as the zooplankton fraction.

4.2.2. Distribution of the zooplankton fraction

Unlike the aggregate volume, the GK10_2 residual volume near the California Current did not go through cycles of sinking and regeneration each day. Instead, the largest V_{res} remained above 3 ppm and oscillated between the surface and 40 m (Fig. 6). The location of maximum V_{res} was deeper during the day (30–40 m) and shallower at night (5–30 m). In all deployments, the mean V_{res} between 5 and 20 m reached maximum values during the afternoon and evening, while lows in mean V_{res} were in the morning (Table 7). The time of maximum V_{res} occurred after that of V_{agg} in most deployments, which differed from the maximum V_{zoo} of TH07_4 that coincided with maximum V_{sno} (Jackson and Checkley, 2011) and V_{agg} . These differences could result from different averaging depths where V_{zoo} was averaged over 5–100 m and V_{res} averaged over 5–20 m.

This pattern of morning lows and evening highs is consistent with diel vertical migration of zooplankton avoiding visual predators (Bollens and Frost, 1989). The dominant zooplankton in this size range (1–6 mm) in and near the California Current are young stages of euphausiids (Brinton and Townsend, 2003), and the copepods *Calanus pacificus* and *Metridia pacifica* (Rebstock, 2001), all of which exhibit diel vertical migration (Bollens et al.,

1992; Dagg et al., 1998). *C. pacificus* and *M. lucens* have been observed at depths below the depth of maximum phytoplankton concentrations in Dabob Bay, Washington (Dagg et al., 1998), such that feeding on aggregates rather than the phytoplankton is plausible. Such behavior has been observed in the subarctic Pacific, where *Neocalanus cristatus* feeds primarily on aggregates sinking out of the euphotic zone (Dagg, 1993).

4.3. Remineralization rates

Changes in aggregate number and size with depth and time are the result of the processes of aggregation (coagulation), disaggregation (fragmentation), remineralization, and feeding (Stemmann et al., 2004a). Aggregation of smaller particles into larger ones increases the number of large particles while decreasing the number of small ones (Jackson, 1990). In contrast, turbulent shear and zooplankton swimming break apart large aggregates (Alldredge et al., 1990; Dilling and Alldredge, 2000), reducing their number and increasing the number of smaller particles. Coagulation and fragmentation do not change the total particle mass, but shift the median particle size. Bacterial remineralization reduces the size but not the number of aggregates, but can weaken them and make them more susceptible to disaggregation. The zooplankton grazing effect on the number-size distribution will depend on the feeding mode. Zooplankton mining of aggregates reduces their sizes similar to the effects of microbes (Steinberg et al., 1997; Iversen and Poulsen, 2007; Poulsen and Iversen, 2008; Poulsen et al., 2011). Filter feeding is proportional to the concentration of particles below a saturating concentration (e.g., Frost, 1972) and preferentially reduces the number of small particles. In contrast, flux feeding is proportional both to the concentrations and velocities of particles and reduces the number of particles with depth more uniformly as a function of size (Jackson, 1993; Jackson and Burd, 2002).

Aggregate volume decreased with depth and time along all 7 subjectively determined sinking trajectories identified in GK10_2 (Fig. 9), but on only 4 trajectories did the median diameter decrease (Table 6). An increase in diameter and decrease in volume (trajectories 3, 4, 7) indicates a decrease in aggregate numbers. This could be the result of aggregation and/or filter feeding. Such sinking events tended to extend deeper into the water column. The aggregates that sank along trajectories 3 and 7 fell in waters with low zooplankton concentrations, as indicated by the small V_{res} there, while aggregates on trajectory 4 sank through depths with large V_{res} (Fig. 6b). The increases in diameter and decreases in volume could result from coagulation being the dominant process along trajectories 3 and 7 and filter feeding along trajectory 4 if we assume that the large-volume zooplankton are doing all the feeding. Smaller protozoa, which are obscured by V_{res} , could also be important grazers (Jackson and Checkley, 2011) responsible for the losses along these trajectories.

On the other hand, the sinking events with negative changes in both volume and diameter (trajectories 1, 2, 5, 6) mark a decrease in aggregate size and number. All of these sinking events had changes in size with time much greater than that of bacterial remineralization (Table 6), thus other processes must have been responsible. These particles resided within and at the base of the mixed layer. Changes in turbulent kinetic energy at the base of the mixed layer could produce shear that would disaggregate marine snow. However, the density interfaces crossed by the particles sinking along trajectories 1 and 2 were very similar to the ones crossed by particles on 3 and 4, thus the density structure does not support both decreased particle sizes on 1 and 2 and increased particle sizes on 3 and 4. As noted in Jackson and Checkley (2011), fragmentation by turbulence in the pycnocline would be evident from a negative correlation between

N_{BV}^2 and V_{agg} , which was not present in GK10_2. Additionally, turbulent kinetic energy in the lower mixed layer was estimated from surface wind speeds following Oakey and Elliot (1982). Turbulent kinetic energy did not exceed the $10^{-3} \text{ cm}^2 \text{ s}^{-3}$ levels that were needed to fragment diatom aggregates in a laboratory experiment (Alldredge et al., 1990).

There were large volumes of residual, zooplankton-like particles near trajectories 1, 2, 5, and 6 (Fig. 6c) suggesting flux feeding preferentially on large, fast-sinking particles as another possible mechanism for the decrease in size with depth. Kjørboe (2000) calculated that zooplankton feeding on aggregates in the mixed layer causes a loss of $0.1\text{--}0.2 \text{ d}^{-1}$ of aggregate POC. This is similar to estimates of microbial effects of $0.075\text{--}0.2 \text{ d}^{-1}$ (Smith et al., 1992; Grossart and Simon, 1998; Ploug and Grossart, 1999, 2000). Combined bacterial remineralization and zooplankton feeding could produce the calculated rates (Table 6). This combination of microbial activity and flux feeding produced model results most consistent with observations of particle spectra from the Mediterranean (Stemmann et al., 2004b). Iversen et al. (2010) estimated remineralization rates, equivalent to our fractional change in volume with depth, that spanned -4×10^{-3} to $-2 \times 10^{-2} \text{ m}^{-1}$ between 40 and 150 m. Their values were smaller than the fractional changes in volume with depth along the sinking trajectories of GK10_2 that ranged from -0.39 to -5.61 m^{-1} . In either case, the values from both these and the Iversen et al. calculations were greater than the values extrapolated from bacterial remineralization rates of roller tank-formed diatom aggregations (Iversen et al., 2010).

Faster remineralization rates and/or slower settling rates indicate greater attenuation of POC with depth, greater attenuation near the surface, and, hence, lower efficiency of the biological pump (Lam et al., 2011). Estimates of remineralization and settling rates were both high along the sinking trajectories of GK10_2 (Table 6). The export efficiency of the system is determined by whichever process, sinking or remineralization, is stronger. In the case of deployment GK10_2, it appears that a large volume of aggregates was exported to at least 100 m (Fig. 7).

In the other deployments the maximum V_{agg} occurred between 10 and 40 m (Fig. 10e, f), but the median diameter often increased until 30–70 m (Fig. 10a, b). Since coagulation alone should not change the total aggregate volume, the increase in size and decrease in volume (numbers) with depth, as occurred in the upper 60 m of deployments NH06, GK10_3, GK10_4, and GK10_7, and the entirety of BL08, NH06, and TH07_1, must have been the result of preferential consumption of smaller aggregates or the combination of coagulation into larger particles followed by consumption. The changes in diameter and volume with depth cannot be attributed to bacterial remineralization or zooplankton consumption without estimation of the remineralization rates for each deployment. A detailed analysis of the deployments will be presented in another manuscript. Here we intended to simply highlight the types of information that may be gained from this method of classifying the aggregate fraction of particles, and how it is consistent with previous studies of marine snow.

4.4. Conclusions

We presented a method of separating the aggregate fraction of particles from LOPC data. The Gaussian-fit fraction correlated highly with *sno*-particles, fluorescence, and POC, suggesting that it was indeed phytoplankton-derived aggregates. The estimated fractal dimensions and settling rates of the aggregate fraction were similar to those reported in the literature for marine snow. Furthermore, depth distributions and daily cycles of aggregate size, concentration, and volume were consistent with in situ observations and simulations of marine snow and known

mechanisms of formation and loss. The residual volume was strongly correlated with *zoo*-particles and exhibited diel vertical migration. The properties of the Gaussian fit and the remaining residual promote the use of this method for separating aggregates and zooplankton from LOPC data and other imaging systems that measure number and size information. This method is especially useful for particles with $d_{0d} \leq 2 \text{ mm}$ that cannot be separated by the relationship between occluded and equivalent spherical diameter. Separated aggregates and zooplankton can be characterized by median diameter, abundance, and volume, which allows for further exploration of spatial and temporal variability. For example, settling rates and fluxes of marine snow can be calculated to attain a high resolution picture of biogeochemical cycling, zooplankton populations can be analyzed for vertical migration, while examination of both allows for the study of particle–zooplankton interactions.

Acknowledgements

This work was supported by NSF Award ID OCE-0927863 to GJ and NSF Award ID OCE03-21167 to DC. Further support was provided by NASA Grant NASA SSC NNX08AI68G. We thank Mike Dagg, a collaborator in the Gatekeeper cruise. We thank Jessica Forest-Baldini for assistance at sea on the Gatekeeper cruise and ashore in the laboratory. We thank Rebecca Asch, Chelsea Didinger, Bill Jones, Steve Rabalais, and Carl Wepking for help at sea. We thank M.J. Perry for the chance to participate in North Atlantic Bloom Experiment on the RV Knorr in 2008 and the CCE LTER program for work on the R/V Thompson in 2007.

References

- Alldredge, A.L., Silver, M.W., 1988. Characteristics, dynamics, and significance of marine snow. *Prog. Oceanogr.* 20, 41–82.
- Alldredge, A.L., Granata, T.C., Gotschalk, C.C., Dickey, T.D., 1990. The physical strength of marine snow and its implications for particle disaggregation in the ocean. *Limnol. Oceanogr.* 35, 1415–1428.
- Ashjian, C.J., Davis, C.S., Gallagher, S.M., Alatalo, P., 2001. Distribution of plankton, particles, and hydrographic features across Georges Bank described using the Video Plankton Recorder. *Deep-Sea Res.* II 48, 245–282.
- Bishop, J.K.B., Wood, T.J., 2008. Particulate matter chemistry and dynamics in the twilight zone at VERTIGO ALOHA and K2 sites. *Deep-Sea Res.* I 55, 1684–1706.
- Bollens, S.M., Frost, B.W., 1989. Zooplanktivorous fish and variable diel vertical migration in the marine planktonic copepod *Calanus pacificus*. *Limnol. Oceanogr.* 34, 1072–1083.
- Bollens, S.M., Frost, B.W., Lin, T.S., 1992. Recruitment, growth, and diel vertical migration of *Euphausia pacifica* in a temperate fjord. *Mar. Biol.* 114, 219–228.
- Brinton, E., Townsend, A., 2003. Decadal variability in abundances of the dominant euphausiid species in southern sectors of the California current. *Deep-Sea Res.* II 50, 2449–2472.
- Checkley Jr., D.M., Davis, R.E., Herman, A.W., Jackson, G.A., Beanlands, B., Regier, L.A., 2008. Assessing plankton and other particles in situ with the SOLOPC. *Limnol. Oceanogr.* 53, 2123–2136.
- Dagg, M., 1993. Sinking particles as a possible source of nutrition for the large calanoid copepod *Neocalanus cristatus* in the subarctic Pacific Ocean. *Deep-Sea Res.* I 40, 1431–1445.
- Dagg, M., Frost, B.W., Newton, J., 1998. Diel vertical migration and feeding in adult female *Calanus pacificus*, *Metridia lucens* and *Pseudocalanus newmani* during a spring bloom in Dabob Bay, a fjord in Washington USA. *J. Mar. Syst.* 15, 503–509.
- Dilling, L., Alldredge, A.L., 2000. Fragmentation of marine snow by swimming macrozooplankton: a new process impacting carbon cycling in the sea. *Deep-Sea Res.* I 47, 1227–1245.
- Engel, A., 2000. The role of transparent exopolymer particles (TEP) in the increase in apparent particle stickiness (α) during the decline of a diatom bloom. *J. Plankton Res.* 22, 485–497.
- Frost, B.W., 1972. Effects of size and concentration of food particles on the feeding behavior of the marine planktonic copepod *Calanus pacificus*. *Limnol. Oceanogr.* 17, 805–815.
- Gorsky, G., Prieur, L., Taupier-Letage, I., Stemmann, L., Picheral, M., 2002. Large particulate matter in the Western Mediterranean I. LPM distribution related to mesoscale hydrodynamics. *J. Mar. Sys.* 33–34, 289–311.
- Grossart, H.-P., Simon, M., 1998. Significance of limnetic organic aggregates (lake snow) for the sinking flux of particulate organic matter in a large lake. *Aquat. Microb. Ecol.* 15, 115–125.

- Guidi, L., Jackson, G.A., Stemmann, L., Miquel, J.C., Picheral, M., Gorsky, G., 2008. Relationship between particle size distribution and flux in the mesopelagic zone. *Deep-Sea Res.* I 55, 1364–1374.
- Herman, A., Beanlands, B., Phillips, E.F., 2004. The next generation of optical plankton counter: the laser-OPC. *J. Plankton Res.* 26, 1135–1145.
- Iversen, M.H., Nowald, N., Ploug, H., Jackson, G.A., Fischer, G., 2010. High resolution profiles of vertical particulate organic matter export off Cape Blanc, Mauritania: degradation processes and ballasting effects. *Deep-Sea Res.* I 57, 771–784.
- Iversen, M.H., Poulsen, L.K., 2007. Coprorhexy, coprophagy, and coprochaly in the copepods *Calanus helgolandicus*, *Pseudocalanus elongatus*, and *Oithona similis*. *Mar. Ecol. Prog. Ser.* 350, 79–89.
- Jackson, G.A., 1990. A model of the formation of marine algal flocs by physical coagulation processes. *Deep-Sea Res.* I 37, 1197–1211.
- Jackson, G.A., 1993. Flux feeding as a mechanism for zooplankton grazing and its implications for vertical particulate flux. *Limnol. Oceanogr.* 38, 1328–1331.
- Jackson, G.A., 1995. Comparing observed changes in particle size spectra with those predicted using coagulation theory. *Deep-Sea Res.* II 42, 159–184.
- Jackson, G.A., Burd, A., 2002. A model for the distribution of particle flux in the mid-water column controlled by subsurface biotic interactions. *Deep-Sea Res.* II 49, 193–217.
- Jackson, G.A., Checkley Jr., D.M., 2011. Particle distributions in the upper 100 m water column and their implications for animal feeding in the plankton. *Deep-Sea Res.* I 58, 283–297.
- Jackson, G.A., Logan, B.E., Alldredge, A.L., Dam, H.G., 1995. Combining particle size spectra from a mesocosm experiment measured using photographic and aperture impedance (Coulter and Elzone) techniques. *Deep-Sea Res.* II 42, 139–157.
- Jackson, G.A., Maffione, R., Costello, D.K., Alldredge, A.L., Logan, B.E., Dam, H.G., 1997. Particle size spectra between 1 μm and 1 cm at Monterey Bay determined using multiple instruments. *Deep-Sea Res.* I 44, 1739–1767.
- Jackson, G.A., Waite, A.M., Boyd, P.W., 2005. Role of algal aggregation in vertical carbon export during SOIREE and in other low biomass environments. *Geophys. Res. Lett.* 32, L13607, <http://dx.doi.org/10.1029/2005GL023180>.
- Kilps, J.R., Logan, B.E., Alldredge, A.L., 1994. Fractal dimension of marine snow aggregates determined from image analysis of in situ photographs. *Deep-Sea Res.* I 41, 1159–1169.
- Kjørboe, T., 2000. Colonization of marine snow aggregates by invertebrate zooplankton: abundance, scaling, and possible role. *Limnol. Oceanogr.* 45, 479–484.
- Kjørboe, T., Andersen, K.P., Dam, H.G., 1990. Coagulation efficiency and aggregate formation in marine phytoplankton. *Mar. Biol.* 107, 235–245.
- Kranck, K., Milligan, T.G., 1988. Macroflocs from diatoms: in situ photography of particles in Bedford Basin, Nova Scotia. *Mar. Ecol. Prog. Ser.* 44, 183–189.
- Lam, P.J., Doney, S.C., Bishop, J.K.B., 2011. The dynamic ocean biological pump: insights from a global compilation of particulate organic carbon, CaCO_3 and opal concentration profiles from the mesopelagic. *Glob. Biogeochem. Cycles* 25, GB3009, <http://dx.doi.org/10.1029/2010GB003868>.
- Lampitt, R.S., Hillier, W.R., Challenor, P.G., 1993a. Seasonal and diel variation in the open ocean concentration of marine snow aggregates. *Nature* 362, 737–739.
- Lampitt, R.S., Wishner, K.F., Turley, C.M., Angel, M.V., 1993b. Marine snow studies in the Northeast Atlantic Ocean: distribution, composition and role as a food source for migrating plankton. *Mar. Biol.* 116, 689–702.
- Logan, B.E., Passow, U., Alldredge, A.L., Grossart, H.-P., Simon, M., 1995. Rapid formation and sedimentation of large aggregates is predictable from coagulation rates (half-lives) of transparent exopolymer particles (TEP). *Deep-Sea Res.* II 42, 203–214.
- Logan, B.E., Wilkinson, D.B., 1990. Fractal geometry of marine snow and other biological aggregates. *Limnol. Oceanogr.* 35, 130–136.
- Lynn, R.J., Simpson, J.J., 1987. The California current system: the seasonal variability of its physical characteristics. *J. Geophys. Res.* 92, 12947–12966.
- MacIntyre, S., Alldredge, A.L., Gotshalk, C.C., 1995. Accumulation of marine snow at density discontinuities in the water column. *Limnol. Oceanogr.* 40, 449–468.
- Mullin, M.M., Sloan, P.R., Eppley, R.W., 1966. Relationship between carbon content, cell volume, and area in phytoplankton. *Limnol. Oceanogr.* 11, 307–311.
- Oakey, N.S., Elliot, J.A., 1982. Dissipation within the surface mixed layer. *J. Phys. Oceanogr.* 12, 171–185.
- Picheral, M., Guidi, L., Stemmann, L., Karl, D., Iddoud, G., Gorsky, G., 2010. The Underwater Vision Profiler 5: an advanced instrument for high spatial resolution studies of particle size spectra and zooplankton. *Limnol. Oceanogr. Methods* 8, 462–473.
- Ploug, H., Grossart, H.-P., 1999. Bacterial production and respiration in suspended aggregates – a matter of the incubation method. *Aquat. Microb. Ecol.* 20, 21–29.
- Ploug, H., Grossart, H.-P., 2000. Bacterial growth and grazing on diatom aggregates: respiratory carbon turnover as a function of aggregate size and sinking velocity. *Limnol. Oceanogr.* 45, 1467–1475.
- Poulsen, L.K., Iversen, M.V., 2008. Degradation of copepod fecal pellets: key role of protozooplankton. *Mar. Ecol. Prog. Ser.* 367, 1–13.
- Poulsen, L.K., Moldrup, M., Berge, T., Hansen, P.J., 2011. Feeding on copepod fecal pellets: a new trophic role of dinoflagellates as detritivores. *Mar. Ecol. Prog. Ser.* 441, 65–78.
- Rebstock, G.A., 2001. Long-term stability of species composition in calanoid copepods off southern California. *Mar. Ecol. Prog. Ser.* 215, 213–224.
- Ruiz, J., 1997. What generates daily cycles of marine snow? *Deep-Sea Res.* I 44, 1105–1126.
- Smith, D.C., Simon, M., Alldredge, A.L., Azam, F., 1992. Intense hydrolytic enzyme activity on marine aggregates and implications for rapid particle dissolution. *Nature* 359, 139–142.
- Steinberg, D.K., Silver, M.W., Pilskaln, C.H., 1997. Role of mesopelagic zooplankton in the community metabolism of giant larvacean house detritus in Monterey Bay, California, USA. *Mar. Ecol. Prog. Ser.* 147, 167–179.
- Stemmann, L., Jackson, G.A., Ianson, D., 2004a. A vertical model of particle size distributions and fluxes in the midwater column that includes biological and physical processes. I. Model formulation. *Deep-Sea Res.* I 51, 865–884.
- Stemmann, L., Jackson, G.A., Gorsky, G., 2004b. A vertical model of particle size distributions and fluxes in the midwater column that includes biological and physical processes. II. Application to a three year survey in the NW Mediterranean Sea. *Deep-Sea Res.* I 51, 885–908.
- Stemmann, L., Prieur, L., Taupier-Letage, I., Picheral, M., Guidi, L., Gorsky, G., 2008. Effects of frontal processes on marine aggregate dynamics and fluxes: an interannual study in a permanent geostrophic front (NW Mediterranean). *J. Mar. Syst.* 70, 1–20.
- Walsh, I.D., Chung, S.P., Richardson, M.J., Gardner, W.D., 1995. The diel cycle in the integrated particle load in the equatorial Pacific: a comparison with primary production. *Deep-Sea Res.* II 42, 465–479.